Rijks*universiteit* Groningen

Faculteit der Wiskunde en Natuurwetenschappen
Natuurkunde

Vakgroep: Fysica van Nanodevices

Towards Spin Injection in Pentacene Thin Films

Master Thesis by:

Eek Huisman

Group Leader: Prof. Dr. Ir. B. J. van Wees

Supervisor: Ir. M. Popinciuc

Referent: Prof. Dr. Ir. P.W.M. Blom

Period: august 2004 - october 2005

Credits: 29 ECTS

MSC plus Materials Science Centre

RuG

Contents

1 Introduction **5**

2 Theory **7**
2.1 Three basic concepts in spintronics 7
2.1.1 Spin injection 7
2.1.2 Conductivity mismatch 7
2.1.3 Non-local measurements 11
2.2 Pentacene 12
2.2.1 Structure 12
2.2.2 Charge transport 13

3 Aspects of making a FSTJ **17**
3.1 Introduction 17
3.2 Surface roughness of cobalt 17
3.3 Anisotropic magnetoresistance of thin cobalt strips 17
3.4 Oxidation of thin aluminum films in air 18
3.5 Conclusions 20

4 Charge transport in pentacene **23**
4.1 Introduction 23
4.2 Charge transport using Ca, Au and Co/AlO_x electrodes 23
4.3 Temperature dependence 25
4.4 Discussion 27
4.5 Conclusions 28

5 Towards spin injection: a non-local measurement **31**
5.1 Introduction 31
5.2 A first attempt: a non-local measurement 31
5.3 Conclusions 33

6 Conclusions **35**
6.1 Conclusions 35
6.2 Prospects 35

A RESISTOR MODEL WITH R_{REL} **37**

B DERIVATION SPACE CHARGE LIMITED CURRENT **41**

C PROPERTIES OF PENTACENE **43**

D PROCESS DETAILS **45**
D.1 General recipe 45
D.2 Chemicals 48
D.3 Processing machines 48

E MEASUREMENT DETAILS **49**

F EXTRA: AN ALUMINUM OXIDE GATE **51**

Chapter 1

Introduction

Our present-day understanding of the electron and its spin has a rich history. The term electron was first proposed in 1894 by the Irish physicist G. J. Stoney [1] as a fundamental unit of electricity. However, the discovery of the electron is usually attributed to J.J. Thomson in 1897, who realized that the electron is a true sub-atomic particle with a finite amount of charge [2]. The electron spin was proposed by Uhlenbeck and Goudsmit in 1925 [3]. They were the first ones to propose that electrons should have an intrinsic angular momentum. Their explanation was closely related to a concept introduced earlier by Pauli in 1924, what he called a "two-valued quantum degree of freedom" for atomic nuclei in order to understand line splitting in atomic line spectra. A few years later, a more precise formulation of the electron including the spin was given by Dirac in 1928 by the formulation of the relativistic wave equation [4]. The notion of spin gave an explanation for several confusing observations, such as anisotropic magnetoresistance in 1857 [5], the Zeeman effect observed in 1896 [6], Stern-Gerlach experiment in 1922 [7] and the anomalies observed in line spectra of atoms.

The electron spin can thus be regarded as the intrinsic angular momentum of an electron, with an associated magnetic dipole. When measured, electron spin can only have two states: spin up and spin down. Since Dirac's formulation in 1928, our conceptual understanding of the electron spin has not changed significantly. However, research on spin-based applications has gained popularity in the last decades and constituted a whole research field called spin electronics or 'spintronics'.

One of the outstanding questions of spintronics is to find a mechanism to create an orientation of electron spins in non-magnetic materials. This is also called spin injection. In non-magnetic materials the spins of (conduction) electrons are oriented randomly, since their two states, up and down, have the same energy in the absence of magnetic fields. If one is able to create an ensemble of oriented spins in these materials, after a time, τ_{sf}, injected spins will randomize due to all kinds of interactions with the magnetic and electric environment of the solid. One of the major sources of randomization of spin is the interaction of spin with the atomic nucleus. Large nuclei will create large fields in the moving frame of an electron, thereby interacting with the spin and randomizing its orientation. Organic materials have relatively light nuclei, which makes them interesting candidates for spin research. Recently, several papers have claimed spin injection in two different organic systems: Alq_3 [8] and sexithiophene [9].

There are several techniques to create oriented spin ensembles in non-magnetic materials. The two most important techniques are optical spin injection and electrical spin injection [10]. We will only consider electrical spin injection. Electrical spin injection was previously experimentally observed in metals [11] [12] and in semiconductors [13] [14]. In contrast to metals, where electrical spin injection was observed using ferromagnetic metals, spin injection in semiconductors has only been observed when using ferromagnetic semiconductors as spin-polarized electrodes. A possible explanation for this has been pointed out in 2000 [15] and is called 'conductivity mismatch' (see section 2.1.2). Conductivity mismatch arises when the conductivity of the non-magnetic material is much lower than the conductivity of the spin-polarized electrodes. One can expect this problem when using ferromagnetic metals, such as cobalt for spin injection in semiconductors, such as GaAs or organic systems. The difference in conductivity makes it impossible to observe spin-injection, when the electrodes and the non-magnetic material are directly connected to each other. The introduction of a tunnel barrier in

between the two can theoretically solve the problem [16] [17].

In this thesis we will focus on pentacene, an organic semiconductor. Research on organic (semi) conductors for making electronic circuits constitutes a field called molecular electronics. Molecular electronics can provide advantages, which conventional electronics cannot offer. The rich chemistry of organics gives an enormous toolbox for modifying materials. Although these materials in general cannot compete with conventional electronic materials in terms of resistivity, mobility and carrier concentration, other properties such as tuneability, flexibility and solubility open doors to new technologies and applications. Pentacene is a molecular crystal and is known for its relatively high mobility (see appendix C). Pentacene has a relative high degree of order and is a convenient material to investigate in going from very ordered (*e.g.* conventional semiconductors) to disordered materials (*e.g.* polymers).

This thesis reports several experiments on the road to spin injection in pentacene thin films and focuses on two important issues for spin injection in pentacene. Firstly, we aim to make cobalt/aluminum oxide/semiconductor junctions, in order to solve the conductivity mismatch problem. For simplicity, we will call these junctions ferromagnet semiconductor tunnel junctions (FSTJs). Secondly, we want to study the charge transport in pentacene thin films with lateral electrode geometry. Although, charge transport in pentacene has been the topic of many research efforts (see for example the references in appendix C), the results of these efforts do not give a consistent picture.

Chapter 2 will shortly discuss basic concepts needed to understand this report. Chapter 3 gives the experimental results of an investigation to make FSTJs. Chapter 4 gives the fabrication and experimental results for lateral devices in order to study the charge transport in pentacene. In section 5 we report our findings on a spin injection experiment. Finally, chapter 6 will give the main conclusions and will give prospects for future research. The appendices give additional information on fabrication and also contains an extra section, section F. This section reports a project, which does not directly connect to the other experiments done for this thesis. It deals with the fabrication of an aluminum oxide gate.

Chapter 2

Theory

2.1 Three basic concepts in spintronics

2.1.1 Spin injection

Our spin injection method makes use of ferromagnetic metals (FM). In these metals the number of conduction electrons with spin up, $n_\uparrow$, is different from the number of electrons with spin down, $n_\downarrow$, resulting in a polarization P:

$$P = \frac{n_\uparrow - n_\downarrow}{n_\uparrow + n_\downarrow}$$

For the 3d FMs iron, cobalt and nickel, P is 0.40, 0.35 and 0.23, respectively [18]. In these materials, spin polarization also results in a current that is spin polarized. The basic idea of spin injection is to send a spin polarized current into an unpolarized material, in this case a semiconductor (SC). A polarization of the current will arise at the interface and decay with increasing distance from the interface. This rate of decay for each material is given by a characteristic length called the spin-flip length, λ_{sf}. Spin injection is schematically represented in figure 2.1.

FMs with a rectangular strip shape have a preferred magnetization, that is orientation of their spins, along the long axis of the strip. The magnetization can be reversed by an external magnetic field applied parallel to the long axis of the strip, thereby reversing the orientation of injected spins. This switching occurs at a certain magnetic field and is dependent on the shape anisotropy (width) of the strip. Spin injection can be observed by a second FM. When sending a current through a FM-SC-FM heterostructure, the voltage drop will be dependent on the relative magnetization of the two FMs. This difference can be directly correlated with spin injection [12]. When using strips of different width for the two electrodes, one can switch the magnetization of the electrodes independently, and obtain a parallel and an anti-parallel orientation of their magnetization.

2.1.2 Conductivity mismatch

In order to explain the conductivity mismatch problem a FM-SC-FM heterostructure is considered and it is assumed that injected spins will maintain their spin state. In practice this means that the distance between the two electrodes, l, is much smaller than the spin-flip length, λ_{sf}. The conduction path through the heterostructure can be divided into two separate channels, one for spin up (up) and one for spin down (down). Each part of the heterostructure in each of the channels has a specific resistance. We assume that the resistance of the semiconductor is spin-independent, R_{SC}. The resistance of the FM depends on the relative orientation of the magnetization of the FM and the orientation of the spin state of the spin channel. The resistance of a parallel orientation, $R_{FM\uparrow\uparrow}$, is lower than the resistance of an anti-parallel orientation, $R_{FM\uparrow\downarrow}$.

Figure 2.2 shows a resistor model for the parallel and anti-parallel configuration of the magnetization of the electrodes. The resistance of each resistor network, R_p and R_{ap}, is given by the inverse of the reciprocal sum of the resistances of the spin up channel, R_{up}, and spin down channel, R_{down}. If one assumes that the resistance of the FM can be neglected compared to the resistance of the SC, the resistance difference, $\Delta R = R_{ap} - R_p$, between the two is zero. ΔR or the expected magnetoresistance

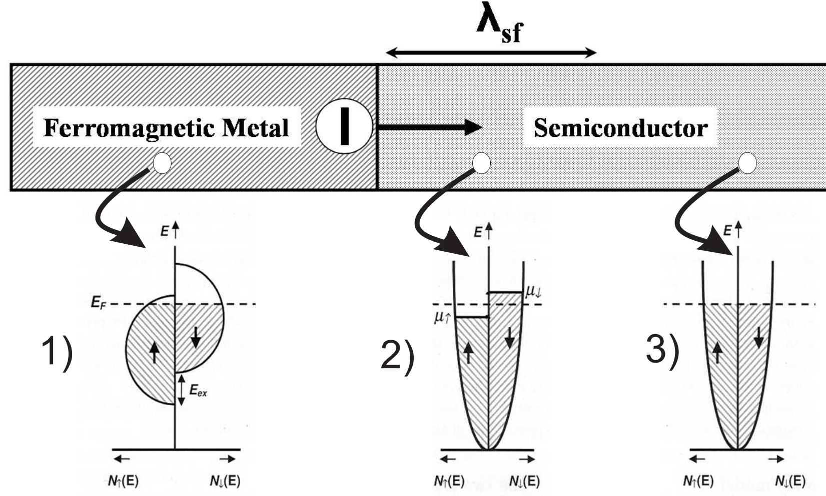

Figure 2.1: Schematic representation of spin injection. A current, I, is sent from a FM to a SC. 1) The conduction band in the FM is split in a spin up band and in a spin down band, having a different density of states at the Fermi energy . 2) The difference in density of states can be maintained in the semiconductor within a distance, λ_{sf}, from the interface. 3) At distances much bigger than λ_{sf}, spins will randomize and the density of states for spin up and spin down are equal.

is the quantity measured in experiments. Typically, the ratio between conductances of the FM and the SC, σ_{FM}/σ_{SC}, is 10^5 for inorganic SC, such as GaAs, and $>10^{10}$ for organic SCs. In this case the picture above is a correct approximation for conventional device geometries and the difference in resistance form a fundamental obstacle for the observation of spin injection, called conductivity mismatch.

A way to circumvent this problem is to introduce a tunnel barrier (TB) in between the FM and the SC [16] [17]. Tunneling is proportional to the overlap in states between both sides of the barrier. This overlap is different for the two spin channels, since the density of states for spin up and spin down are different in the FM. This results in a different effective resistance if the direction of the spin in the spin channel and the magnetization of the TB is parallel, $R_{TB\uparrow\uparrow}$, or anti-parallel, $R_{TB\uparrow\downarrow}$. $R_{TB\uparrow\uparrow}$ and $R_{TB\uparrow\downarrow}$ are roughly given by:

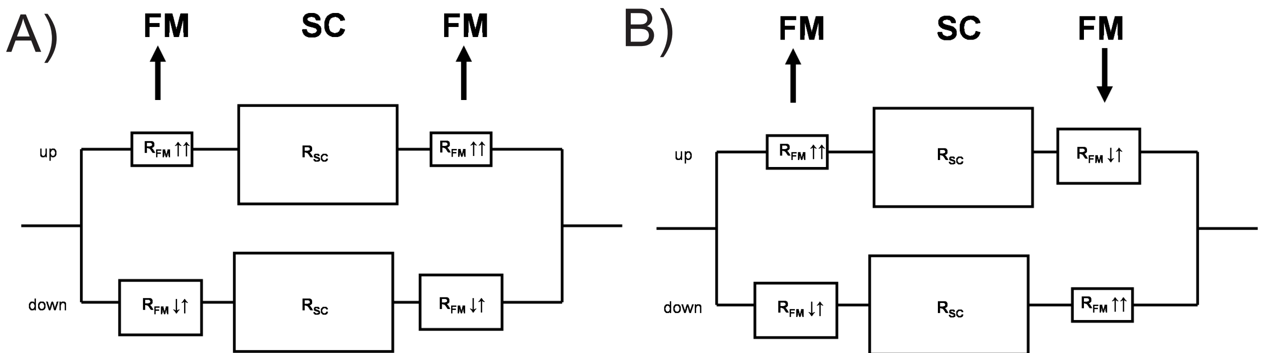

Figure 2.2: Resistance model of a FM-SC-FM heterostructure with a parallel configuration, A, and an anti-parallel configuration, B, of the magnetization of the FMs. For $R_{SC} >> R_{FM}$ clearly, the difference in resistance between the two configurations is negligible.

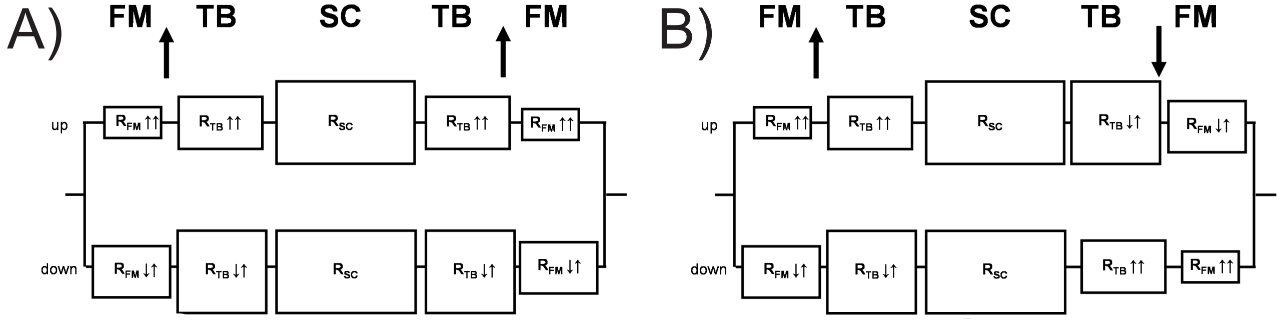

Figure 2.3: Resistance model of a FM-TB-SC-TB-FM heterostructure with a parallel configuration, A, and an anti-parallel configuration, B, of the magnetization of the FMs. For $R_{SC} >> R_{FM}$, the difference in resistance between the two configurations is non-negligible.

$$R_{TB\uparrow\uparrow} = \frac{R_{TB}}{1+P}$$

$$R_{TB\uparrow\downarrow} = \frac{R_{TB}}{1-P}$$

Figure 2.3 shows the different situations for a parallel and anti-parallel configuration of the electrodes. Again, we can calculate the resistances of both configurations. From this simple resistance model one can calculate the expected normalized magnetoresistance:

$$\frac{\Delta R}{R_p} = \frac{4R_{TB}^2P^2}{(P-1)(P+1)(R_{SC}P - R_{SC} - 2R_{TB})(R_{SC}P + R_{SC} + 2R_{TB})}$$

Figure 2.4 gives $\frac{\Delta R}{R_p}$ as a function of $\frac{R_{SC}}{R_{TB}}$ for polarization factors typical for 3d FMs. In this simple model, one clearly sees that the magnetoresistance becomes non-zero when $R_{TB} > 0.1R_{SC}$ and the conductivity mismatch problem is solved. The magnetoresistance saturates at lower values of $\frac{R_{SC}}{R_{TB}}$.

The simple model described above is idealistic, since we assume that the electrode spacing is much smaller than the spin flip length in order to neglect relaxation of spins inside the SC. In reality this is not valid. It is expected that the polarization has an exponentially decay with distance from the metal-SC interface [12]. A simple way of including relaxation in our simple resistor model is to add a resistance in between the two channels, R_{REL}, see figure 2.5. A derivation of the following two equations can be found in appendix A. One can show that the expected magnetoresistance is given by:

$$\frac{\Delta R}{R_p} = \frac{8R_{TB}^2R_{REL}P^2}{(2R_{TB} + R_{SC} + R_{SC}P)(2R_{TB} + R_{SC} - R_{SC}P)(2R_{TB} + R_{SC} - R_{SC}P^2 + R_{REL} - 2R_{REL}P^2)} \quad (2.1)$$

in which R_{REL} is given by:

$$R_{REL} = \frac{R_{SC}exp(\frac{-L}{2\lambda_{sf}})}{(1 - exp(\frac{-L}{2\lambda_{sf}}))^2} \quad (2.2)$$

Figure 2.6 gives $\frac{\Delta R}{R_p}$ as a function of $\frac{R_{SC}}{R_{TB}}$, for different fractions of $\frac{L}{\lambda_{SF}}$. Again, one clearly sees that the magnetoresistance becomes non-zero when $R_{TB} > 0.1R_{SC}$ and the conductivity mismatch problem is solved. However, now the magnetoresistance does not saturate, but becomes zero again at lower values of $\frac{R_{SC}}{R_{TB}}$ when the distance between the electrodes increases.

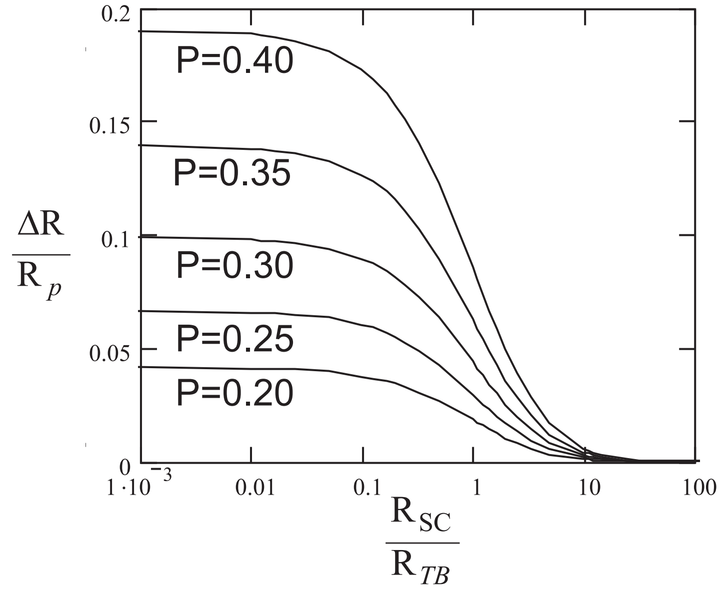

Figure 2.4: Normalized magnetoresistance versus $\frac{R_{SC}}{R_{TB}}$ for various values of P for the resistor network of figure 2.3. One can clearly see that the conductivity mismatch problem is solved for values $R_{TB} > 0.1R_{SC}$.

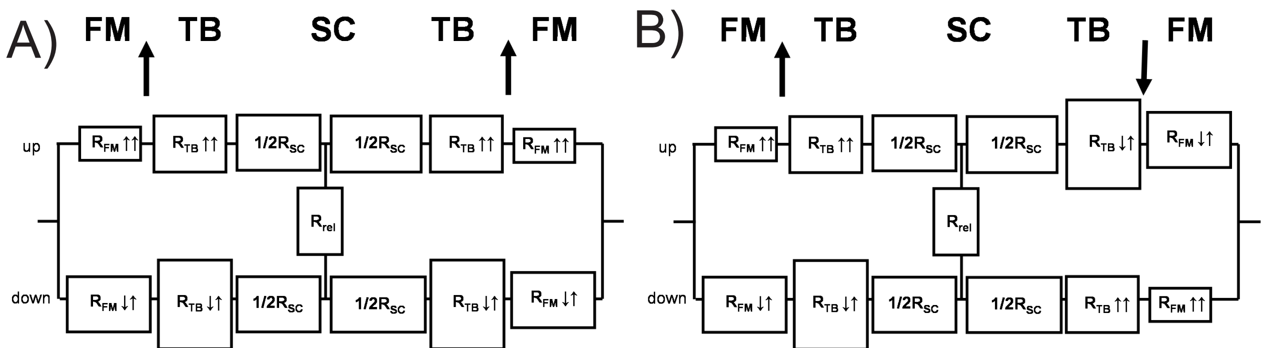

Figure 2.5: Resistance model of a FM-TB-SC-TB-FM heterostructure including relaxation with a parallel configuration, A, and an anti-parallel configuration, B, of the magnetization of the FMs. For $R_{SC} >> R_{FM}$, the difference in resistance between the two configurations is non-negligible and is dependent on λ_{sf}.

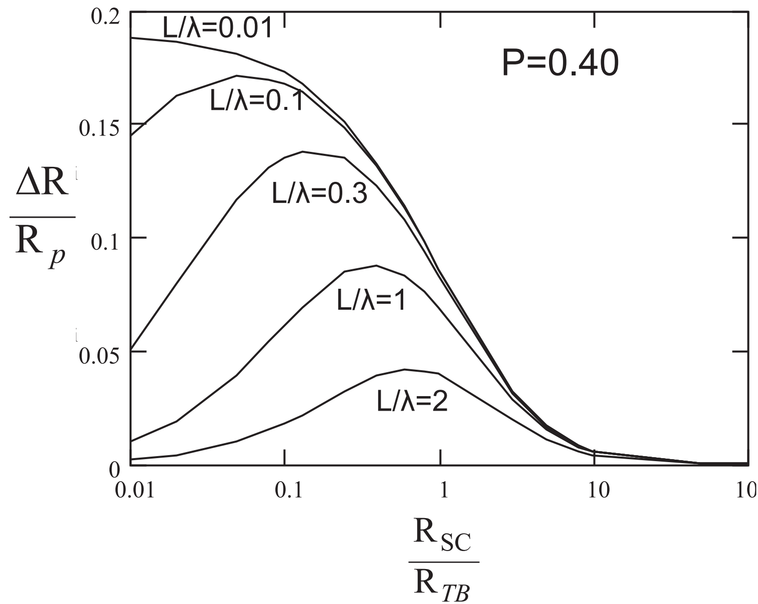

Figure 2.6: Normalized magnetoresistance versus $\frac{R_{SC}}{R_{TB}}$ for various values of $\frac{L}{\lambda_{SF}}$ and P=0.40 for the resistor network of figure 2.5. One can clearly see that the conductivity mismatch problem is solved for values $R_{TB} > 0.1R_{SC}$. However, the magnetoresistance goes to zero again at lower values of $\frac{R_{SC}}{R_{TB}}$ when relaxation becomes more important.

2.1.3 Non-local measurements

An important requirement in spintronics is to separate spin effects from other effects. Typical for electrical spin injection experiments is to look for a change in the resistance as a function of magnetic field, also called magnetoresistance. Effects, which have nothing to do with spin injection can also give rise to magnetoresistance. For example ferromagnetic electrodes produce magnetic fields and can cause Hall effects. Also, the electrodes themselves can give rise to anisotropic magnetoresistance (AMR). A special measurement geometry, called the non-local geometry can separate spin injection effects from the other effects.

A possible configuration is given in figure 2.7. A simple explanation of the idea behind this method can be given as follows. When injecting spins, a spin imbalance is created at the injecting contact. This spin imbalance will decay with distance from the interface and hence a spin density gradient will arise, which will cause spin diffusion. In contrast to two probe measurements, where voltage probes sense both the potential drop in the SC and the magnetoresistance, non-local 4-probe measurements do not measure the potential drop in the SC. In the absence of an applied electric field, spin diffusion is not accompanied by a net charge current, since an equal amount of spins up travel to the right as compared to spins down to the left. This is because the chemical potential of spin up is lowered with the same amount as the chemical potential of spin down is raised. Therefore, outside the electrodes where the electric field is applied, E=0 and $\frac{dn_{\uparrow,\downarrow}}{dx} \neq 0$. Or, in other words: there will be a net zero charge current and a non-zero spin current. This current can be detected by a spin dependent voltage probe like a FM. For our non-local measurement we use four ferromagnetic electrodes, such as given in figure 2.7. A spin imbalance is created in the material by sending a current between the first two electrodes. The voltage drop between the third and fourth electrodes is then measured. These voltage probes are located within the spin-flip length of the closest of the first electrodes. Between the voltage probes, a spin gradient, but no electric field is present. A voltage will be sensed due to this spin gradient. This voltage is then completely due to spin currents and not due to charge currents. This measurement geometry is also called 'non-local' geometry. The spin signal in a non-local measurement should reverse sign while switching the magnetization of one of the electrodes. In metals and carbon nanotubes, this has been observed experimentally [12] [19]. An important practical condition for multiple probe measurements is that they require a so called lateral device geometry, see section 2.2.2.

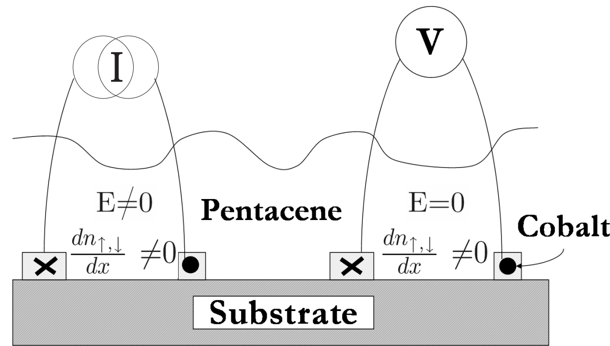

Figure 2.7: Schematic picture of a non-local measurement geometry with four FM electrodes. The magnetization of the electrodes is either directed out of the paper (dot) or in the paper (cross). A current is sent between the left two electrodes and both an electric field and a spin gradient are present. Voltage is measured between the left two electrodes. No electric field is present. However, a spin gradient is still present if the electrodes are located within the spin-flip length of the first electrodes. This spin gradient gives rise to a voltage between the two FM electrodes. The measured voltage should reverse sign when the magnetization of one of the electrodes is switched.

2.2 Pentacene

2.2.1 Structure

Pentacene ($C_{22}H_{14}$) contains only carbon and hydrogen atoms. Its structure is represented in figure 2.8. Pentacene belongs to a group of molecules called polycyclic aromatic hydrocarbons [20]. Molecules of this group have several hydrocarbon rings in which the carbon atoms are alternatingly connected by carbon double and single bonds. More specifically, pentacene is the fifth member in the group of fused benzene rings in a linear arrangement, called the acenes. The first four members are benzene, naphtalene, anthracene and tetracene. Above five rings a linear arrangement becomes less stable and therefore less abundant.

The alternation of double and single bonds, also called conjugation, is a result of a specific atomic electronic configuration. In general the electronic configuration of carbon is given by $2s^2 2p^2$. In conjugated structures two of the three p orbitals of the carbon atom hybridize with the s orbital to form 3 spatially localized orbitals. The three orbitals are located in the same plane and the angle between the orbitals is equal, 120°. These orbitals are mainly responsible for chemical bonding between carbon atoms. The p orbital left, usually called the p_z orbital, is spatially localized above and below this plane. In conjugated systems these p_z orbitals also contribute to chemical bonds in the plane. However, such a bond is much weaker than bonds made from the hybridized orbitals. Therefore, these electrons can also contribute in electronic conduction. This explains the relatively high conductivity of a sheet of graphene.

Thermodynamically speaking, pentacene is quite stable. When storing at room temperature in air only one significant impurity species will form, 6,13-pentacenequinone. This species is quite different from pentacene itself due to the attachment of two oxygen atoms and has lost its full conjugation. The quinone can be removed by vacuum sublimation. Pentacene is a crystalline solid at room temperature. In general, pentacene crystals have a triclinic crystal system and have four distinguishable phases or symmetries [21]. Crystals are composed of layers, in which the long axis of the molecule is oriented almost perpendicular to the plane of the layer. In-plane pentacene molecules are arranged in a herringbone-like way, as can be seen in figure 2.9. The relative orientation of the hydrogen atoms between molecules and the angle of the long axis with respect to the plane determine the specific phase of the crystal. Phases are characterized by the spacing between stacked layers, d. The four phases are characterized by d-values of 1.41 nm, 1.45 nm, 1.50 nm and 1.54 nm. Thin films structures can depend on temperature and substrate and the 1.41 nm is most likely to form. Single crystals of pentacene can be grown by vapor transport growth [22]. Thin films of pentacene show an island-type

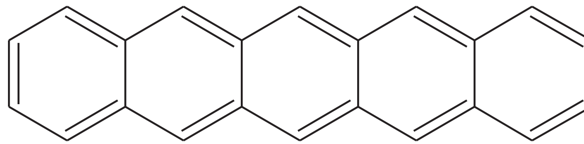

Figure 2.8: Representation of pentacene. Each line represents a carbon-carbon bond and each intersection of lines corresponds to a carbon atom. For simplicity, the hydrogen atoms are omitted here.

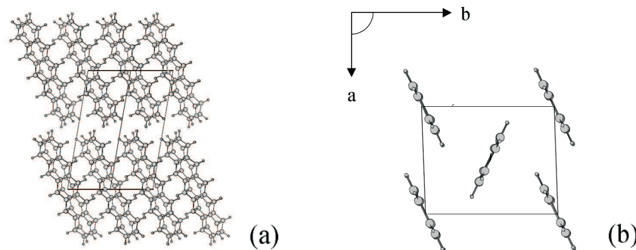

Figure 2.9: Stacking of pentacene molecules in the crystal. Pictures are taken from Mattheus [21]. a) Stacked layers of pentacene molecules, viewed along the $[1\bar{1}0]$ axis. For clarity a unit cell is drawn. b) Projection of the pentacene crystal structure on a plane perpendicular to the molecular axis. The herringbone arrangement is clearly visible.

growth mode (Stranski-Krastanov), resulting in thin films composed of crystalline grains with typical dimensions of several micrometers depending on substrate and substrate temperature during or after deposition [23]. Some properties of pentacene are summarized in table C.1 in appendix C.

2.2.2 Charge transport

Space charge limited current

How to think about charge transport in pentacene? Lets consider the problem in a band picture. Pentacene has a filled valence band (or in molecular terms highest occupied molecular orbital, HOMO) separated from an empty conduction band (in molecular terms lowest unoccupied molecular orbital, LUMO) by a band gap of 2.2 eV which is much larger than k_bT=0.03eV (298K). One can inject carriers by either injecting electrons in the conduction band or holes in the valence band. We consider one carrier injection, since pentacene is a hole conductor, or p-type semiconductor.

Metals, usually have a lot of intrinsic carriers which are free to move throughout the material, since there are many empty states just above the Fermi level. Pure semiconductors have a band gap and the the number of charge carries is limited. Injecting a charge carrier in a semiconductor will give rise to a so called space charge. An increase in the electric field will inject more charge carriers, which space charge will increase the electric field even more giving rise to a current which is quadratically dependent on voltage. The current will be bulk limited. This is in contrast to Ohmic conductors which have a linear dependence on voltage and are injection limited. The quadratic behavior is also known as space charge limited current (SCLC) and is described by the Mott-Gurney law, also known as Child's law:

$$J = \frac{9}{8}\mu\epsilon\frac{V^2}{L^3} \tag{2.3}$$

Here, J is the current density, μ is the mobility, V is the voltage and L is the electrode spacing. A derivation can be found in appendix B. Pentacene single crystals obey this space charge limited behavior [22]. Note that the only material parameters characterizing the charge transport in the equation above is the mobility and the (local) dielectric constant.

The influence of non-idealities on charge transport

This section will qualitatively describe the influence of three non-idealities on charge transport in pentacene which are important in our case:

- The influence of **traps**
- The influence of the **electrode geometry**
- The influence of the **electrode material**

Traps

The band model above assumes a SC with a gap without (impurity) states in the gap. In reality states will be present. For pentacene thin films the most well known impurities causing trap states in the band gap are water, oxygen and grain boundaries between crystalline islands [22] [24] [25] [26] [27]. The effect of water and oxygen on charge transport are described by Jurchescu *et al.* [24]. Air can reversible diffusive in pentacene and affects electrical transport significantly. Water reduces electrical transport, because its electric dipole induces energetic disorder and traps charge carriers. Oxygen on the other hand enhances electrical transport and attracts electrons, thereby forming holes. The effect of oxygen can even be enhanced in the presence of light. When exposing a pentacene layer in ambient air to light, current increases by about a factor of two. The polycrystalinity in pentacene thin films causes a non uniform dielectric medium. Minari *et al.* [28] report an enhancement of mobility (and current) in pentacene thin-film transistors when they are made from a single grain as compared to polycrystalline ones.

The presence of traps can be accounted for in the SCLC model. A ratio, Θ, of free carriers to the total number of carriers [21] can be defined.

$$\Theta = \frac{n_{free}}{n_{free} + n_{trapped}} = \frac{gN_v}{N_t} e^{\frac{-E_t}{k_b T}}$$

Here g is the degeneracy factor of the traps (1/2), N_v is the effective density of states in the valence band (usually assumed to be 1 per molecule = $4.3 \cdot 10^{21}$ cm^{-3}) and E_t is the energy of the trap with respect to the Fermi energy. In the trap filled limit, Θ=1. To implement it in the SCLC model, one can simply multiply the factor with the expressions for J given above.

Electrode geometry

To investigate charge transport one can contact a material in several ways. Because of the relative high resistivity of organic SCs, the contact resistance and the resistance of the leads can often be neglected. The most straightforward way of applying contacts to a piece of material is to clamp a thin sheet of material between two electrodes such that the current is flowing perpendicular to the sheet. A major advantage of this geometry is the electric field uniformity. Also, one can easily make large contact areas (A) and thin films (L) such to increase the total current, since $R \propto \frac{L}{A}$.

Another geometry can be obtained by connecting a sheet of material laterally. In a lateral geometry, the electrodes are attached on top or below the sheet of material such that the current is flowing in the plane of material. The ultimate advantage of this geometry is that one can use multiple electrodes, which is one of our demands. However, the conductance path in this geometry is not well defined since the electric field is not completely homogeneous [29]. The non-uniformity of the electric field in a lateral geometry is caused both by the electrode shape, usually a strip with sharp edges, and by the influence of the substrate. Lateral geometries can be made either by applying electrodes on top or below a film. Applying electrodes on top of pentacene might damage the pentacene and cause an ill defined metal-electrode interface [30].

Electrode material

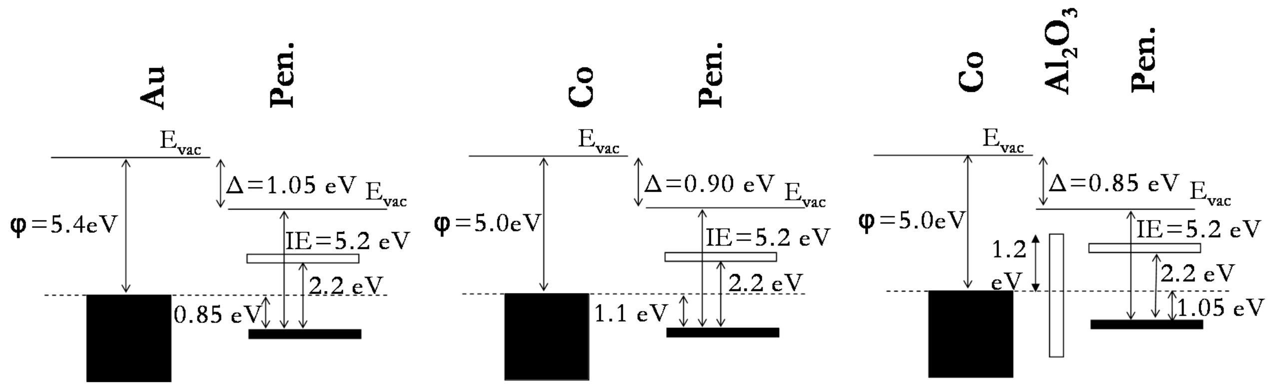

Figure 2.10: Band pictures of pentacene connected to gold, cobalt and cobalt/aluminum oxide, respectively. The band picture predicts the effective hole injection barriers. The Fermi level is indicated by the dotted line. Cobalt and aluminum oxide data is obtained from UPS measurements [31], gold data is obtained from Koch *et al.*[34] and aluminum oxide barrier height is obtained from [35]. IE is the ionization energy and Δ is a dipole that arises at pentacene-metal interfaces, which will effectively change the vacuum level.

Pentacene is a hole conductor, since the cation of pentacene (a pentacene molecule missing one electron) is more stable than the anion of pentacene (a pentacene molecule with one additional electron). The easiest way to inject holes in pentacene is to connect it with an electrode which Fermi level is close to the HOMO of the pentacene. We use the same electrode material for the cathode and the anode: gold, cobalt and cobalt/aluminum oxide. Schematic energy diagrams of these three situations without bias are given in figure 2.10. In this picture we assume that pentacene maintains its molecular properties, such that the levels are not broadened. Due to a dipole at metal-pentacene interfaces the electrons in both materials experience a different vacuum level. This dipole is formed due to electron transfer from pentacene to the metal. The contacts in the simplified model of figure 2.10 are clearly non-Ohmic and a hole-injection barrier appears of 0.85 eV and 1.1 eV for a gold/pentacene and a cobalt/pentacene interface, respectively. When introducing a tunnel barrier in between the metal and the pentacene, a dipole will be formed between the oxide and the pentacene. However, the dipole between the pentacene is strongly reduced [31]. For AlO_x this results in an effective hole injection barrier of 1.05 eV [31]. Note, that in this case the conduction mechanism is different, due to the presence of a tunnel barrier. Now, charge carriers can cross this barrier by an inelastic tunnel process. In the band picture, at high positive biases a triangular shaped electron barrier arises and one might expect electron injection. Pentacene field effect transistors using both hole and electron injection contacts report pronounced increase of drain currents at large values for the drain-source voltage [32] [33].

Chapter 3

Aspects of making a FSTJ

3.1 Introduction

In order to circumvent the conductivity mismatch problem we aim to make ferromagnet semiconductor tunnel junctions (FSTJs) from cobalt, aluminum oxide and pentacene. In this chapter we investigate the feasibility of such a tunnel junction. Earlier research on these junctions showed that in order to prevent pinholes in the aluminum oxide layer, the surface roughness of the substrate should be less than 0.3 nm RMS [36]. Therefore, we have to use thin cobalt layers (typically 10 nm) and an appropriate substrate. First we investigate the surface roughness of cobalt thin films on several substrates. Then we will investigate the switching behavior of thin cobalt rectangular strips by measuring the anisotropic magnetoresistance (AMR) of these films. Finally, we will report our findings on making thin aluminum oxide layers on cobalt electrodes by oxidizing aluminum layers and show their electrical properties. Aluminum layers were oxidized in air and by an oxygen plasma.

3.2 Surface roughness of cobalt

We used atomic force microscopy (AFM) under ambient conditions to investigate the roughness of several structures of 1.0 μm^2 on top of a clean SiO_2 substrate (silicon quest international 500 nm SiO_2, boron doped, 1-10 Ωcm). We investigated two ways of material deposition: evaporation and sputtering. Evaporation was done with a Temescal e-gun evaporation system in a vacuum chamber with a base pressure of $5 \cdot 10^{-7}$ mbar. Sputtering was done on a Leybold Hereaus Z400 system in a vacuum chamber with a base pressure of $2 \cdot 10^{-6}$ mbar (48 W, $p_{argon} = 4 \cdot 10^{-2}$ mbar). The results are given in table 3.1. Efforts to also sputter thin layers of aluminum and aluminum oxide did not succeed, because the sputter rate could not be controlled at low rates. Samples with aluminum have been exposed to air, such that an oxide layer will form on top of the aluminum. The results show that thin evaporated ($\approx$ 7nm) cobalt layers can be used on top of clean SiO_2 without the use of a (tantalum) wetting layer to get a smooth cobalt surface. Furthermore, it can be seen that the roughness of the native aluminum oxide layer on top of an aluminum layer of about 6 nm is in the order 0.5-0.6 nm RMS.

3.3 Anisotropic magnetoresistance of thin cobalt strips

To investigate ferromagnetic switching of 9 nm thick cobalt rectangular shaped strips, the resistance of these strips was measured as a function of magnetic field. The switching of a ferromagnetic bar is dependent on the width of the bar. Since the resistance of a ferromagnet depends on the orientation of the magnetic domains inside the ferromagnet, we can observe switching while monitoring the resistance. This magnetoresistance is also known as anisotropic magnetoresistance (AMR)[1].

Electrode patterns were made by optical lithography, electron beam lithography and e-gun metal evaporation in a vacuum chamber with a base pressure of 10^{-7} mbar. A general recipe for sample

[1]The theory of AMR is not treated in this report and can be found elsewhere [37].

fabrication and more details about processing machines can be found in appendix D. A scanning electron microscope (SEM) image of a typical device is given in figure 3.1. The strips have a length of 12 μm and widths of 240, 287, 476, 867 and 1640 nm, respectively.

Resistance was measured by sending a 10 μA DC current through the outer most electrodes, while measuring the voltage drop between the inner two electrodes. A magnetic field was applied with a tabletop magnet in plane with the strip both parallel and perpendicular to the long axis of the strip. A typical measurement is given in figure 3.2.

All curves have a continuous resistance change, indicating single domain switching. The resistance change in perpendicular geometry is typically 0.3 % of the total resistance, which is about 3 times smaller than the 0.8 % reported elsewhere for 40 nm thick cobalt strips [12]. The switching field was determined by taking the minimum of resistance in the parallel geometry (figure 3.2b). Switching field as a function of width is plotted in figure 3.3. Switching fields are roughly four times smaller than switching fields reported for cobalt strips with a thickness of 60 nm [38]. This is consistent with an experiment found in literature [39].

A reduction in the relative value of AMR of thin strips compared to thick strips can be justified qualitatively. When reducing the height of a strip, the surface/volume ratio is highly increased. This might cause a strong reduction of the anisotropic effect, if surface parts of the sample contribute less to the AMR effect. In our experiment, cobalt was exposed to air, such that a thin (+/- 1nm) layer of cobalt oxide forms at the surface. Cobalt oxide is anti-ferromagnetic and might diminish the anisotropic magnetoresistance due to pining of magnetic domains in the underlying cobalt layer. Note that cobalt oxide has a resistivity of $1.0 \cdot 10^6 \Omega$m [40] and is not likely to form a more favorable conduction path compared to the cobalt. Also, it is known that the domain wall type in permalloy strips changes from a Bloch to a Néel wall between 35 and 30 nm [41] when reducing the height of a strip. For a Bloch wall, the magnetization rotates in the plane of the strip during switching. For a Néel wall, the magnetization rotates out of the plane. To the best of our knowledge, the domain wall type transition is not reported for cobalt. However, if present it is likely to affect the relative value of the magnetoresistance and the value of the switching field.

3.4 Oxidation of thin aluminum films in air

We made a FM-TB-N-TB-FM (N=metal) hetero structure by using the same patterns as described above, according to the general recipe given in appendix D. Note that our devices always have to be transported through air, since a lift-off step in solution is required for making the electron beam lithography patterns. This limits the height of the aluminum layer, since the oxidation process of aluminum in air will form about 1 nm of aluminum oxide in only several minutes.

We chose to make heterostructures of 9 nm of cobalt and 2 nm of aluminum. The samples were oxidized in air for 20 minutes and exposed to an oxygen plasma (50 s, 40 W, 9 sccm, 9 μbar) in order to oxidize the aluminum. Atomic force microscopy (AFM) showed that the structure had a height

Table 3.1: Roughnesses of several thin structures of 1.0 μm^2 on top of a clean SiO_2 as determined by AFM, roughnesses marked with a star are determined with a different AFM tip.

Material	Roughness (nm RMS)	**S**puttered/**E**vaporated
Clean SiO2	0.232	-
15 nm Co	0.491	S
7 nm Co	0.228*	E
20 nm Co + 4 nm Al	0.584	E
6 nm Al	0.541	E
10 nm Ta	0.302, 0.250*	E
10 nm Ta / 4 nm Al	0.528	E
8 nm Ta / 7 nm Co	0.292	E

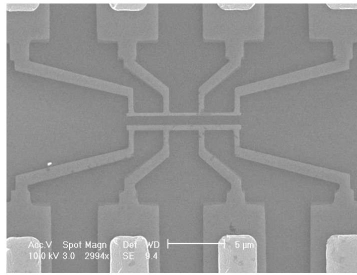

Figure 3.1: SEM image of two cobalt 9 nm high strips (240 nm and 476 nm wide) contacted to 4 probes to measure the resistance as a function of magnetic field. The two inner probes are used to measure the voltage, the two outer probes are used to send the current.

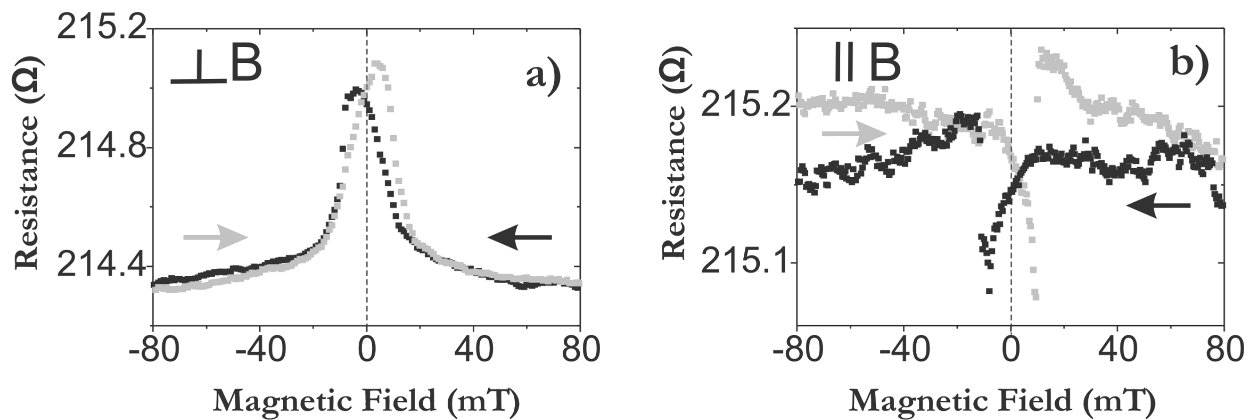

Figure 3.2: Typical 4-probe resistance measurement of a 9 nm thick cobalt rectangular shaped strip as a function of a) perpendicular magnetic field and b) parallel magnetic field. The width of the strip is 867nm. Grey data points corresponds to an up-sweep of magnetic field, black corresponds to a down-sweep of magnetic field. The drift in signal in b) is caused by heating of the sample while measuring.

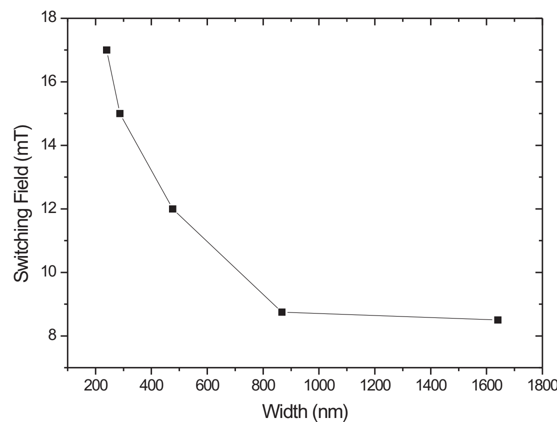

Figure 3.3: Switching field as a function of strip width of 9 nm high rectangular shaped cobalt strips. The switching field corresponds to the minimum in the magnetoresistance while applying a magnetic field parallel to the long axis of the strip, see figure 3.2b.

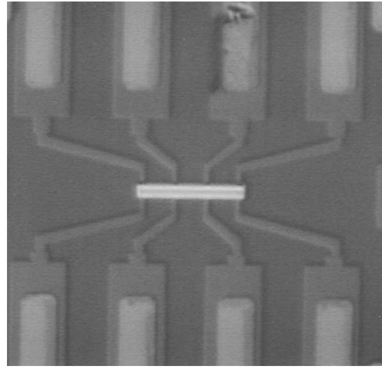

Figure 3.4: Optical microscope image of two cobalt/aluminum oxide electrodes covered by an aluminum strip of 40nm. The size of the aluminum strip is 14 x 2 μm^2. And the width of the underlying electrodes are 240 nm and 502 nm and are separated by 310 nm.

of 11.75 nm and a roughness of about 0.3 nm RMS (0.2 μm^2) after oxidation. If only the aluminum oxidizes, this means that aluminum expands by a factor of 1.4. An additional AFM measurement of a pattern of 1.0 nm of evaporated aluminum showed a height after oxidation in between 1.4 and 2.0 nm. This is close to the value of 1.5 reported elsewhere [42] and close to the expansion factor expected for stoichiometric Al_2O_3 (1.3). However, it is also expected that for aluminum layers of 2.0 nm on top of cobalt, cobalt will oxidize before stoichiometric Al_2O_3 has formed [42]. The formation of cobalt oxide cannot be completely excluded.

On top of the cobalt/aluminum oxide junction, a strip pattern was made by electron beam lithography and 40nm of aluminum was deposited by e-gun evaporation (see appendix D). An optical microscope picture of this device is given in figure 3.4. Underneath the aluminum strip, two cobalt/aluminum oxide strips with widths of 240 nm and 502 nm separated by 310 nm are present. The sample was glued to a 12-pins sample holder, bonded and connected to a multimeter. The current-voltage characteristic when sending a voltage between the two electrodes, while measuring the current is given in figure 3.5.

The experimental data can be fitted by Stratton's formula [43] [44] in a simplified form [45]:

$$I(V) = I_0 sinh\left[\frac{eV\tau}{\hbar}\right]$$

Here, I_0 is a constant, e is the electron charge and $\hbar$ is Plancks constant. $\tau = w/\sqrt{2U/m}$, the tunneling traversal time where U is the barrier height, w the barrier thickness and m is the free electron mass. Our data fits with τ=3.5 fs. If we assume that in this case each barrier has a barrier height of 1.2 eV [35], d = 2.3 nm which corresponds to a aluminum oxide thickness of 1.2 nm for each barrier, which is reasonable in agreement with what we expect. The resistance at zero bias is about 8 GΩ.

3.5 Conclusions

The possibility of making FSTJs has been investigated. AMR measurements showed that switching field of magnetization reversal in rectangular cobalt strips with a height of 9 nm can be controlled by an external magnetic field by changing the width of the strips. The relative value of the AMR when switching the magnetization by a magnetic field applied perpendicular to the long axis of the strip was found to be 0.3 %. Switching fields of 8-17 mT were found for strips with a widths of 1640-240 nm when reversing the magnetization along the long axis of the strips. By oxidizing cobalt/aluminum heterostructures, closed oxide layers were formed on top of heterostructures of 9/10 nm cobalt and 2 nm aluminum. Current voltage characteristics of a FM-TB-N-TB-FM junction, clearly showed tunneling behavior. A simple fit of the data gave a barrier thickness of 1.2 nm, which is in the same order of magnitude as the measured aluminum oxide barrier thickness (2-3nm). The oxide layers form tunnel barriers with typical resistances of a few GΩ at zero bias in our devices.

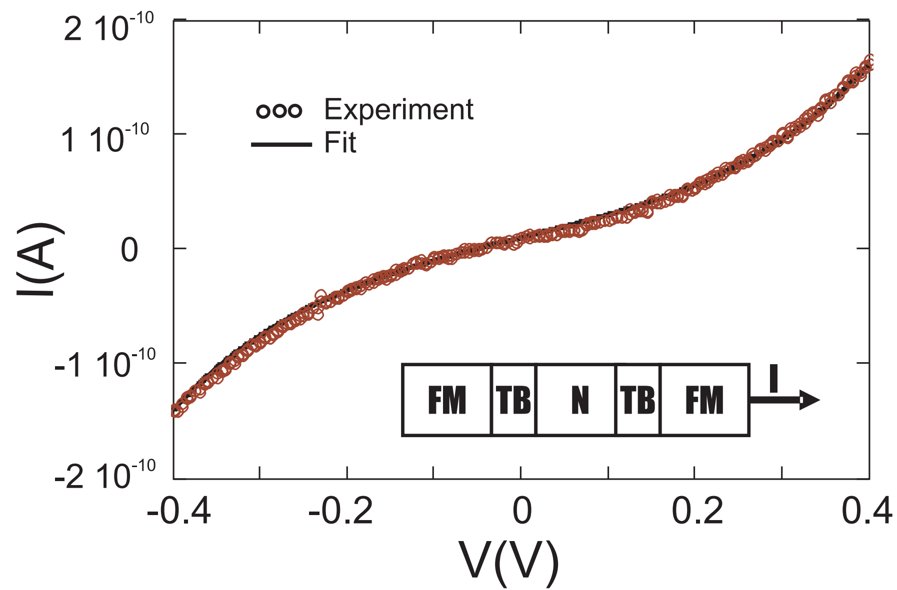

Figure 3.5: Current voltage characteristic of a FM-TB-N-TB-FM (N=metal) heterostructure. FM are cobalt strips of 9nm with widths of 240 and 502 nm, respectively. TB are aluminum oxide barriers of approximately 2 nm thick. N is a strip of aluminum on top of the electrodes, see figure 3.4. The experiment (open circles) can be fitted by equation 3.4 (solid line).

Chapter 4

Charge transport in pentacene

4.1 Introduction

In this chapter, we report our experimental procedures and results on charge transport measurements of pentacene thin films in a lateral device geometry. Although, charge transport in pentacene has been the topic of many research efforts (see for example the references in appendix C), the results of these efforts do not give a consistent picture. We have investigated charge transport in devices with clean electrodes (cobalt and gold) and electrodes with tunnel barriers (cobalt/aluminum oxide). The influence of the electrode material and the temperature dependence of charge transport have been investigated. Understanding charge transport is a crucial step on the road to spin injection experiments.

4.2 Charge transport using Ca, Au and Co/AlO$_x$ electrodes

A general recipe for sample fabrication and more details about processing can be found in appendix D. Electrode patterns were made by optical lithography, electron beam lithography and e-gun metal evaporation in a vacuum chamber with a base pressure of $5 \cdot 10^{-7}$ mbar. Several batches of samples with electrodes of different materials (5 nm Ti/25 nm gold, 25 nm cobalt and 10 nm cobalt/1.8nm aluminum) were fabricated. The electrodes were deposited in a so called 'finger' pattern. An optical microscope image of a finger electrode pattern is given in figure 4.1a. The sample was designed in this way to maximize the electrode surface. The pattern can be regarded as 22 parallel electrode pairs with a an effective width, w, of 10 μm and a spacing, l, of 300 nm. After electrode patterning, the samples were transferred to an ultra high vacuum (UHV) system through air. Cobalt will get oxidized when exposing to air. The removal of about 4/5 of the native cobalt oxide layer by two hours of in-situ argon ion milling was verified by in situ X-ray photo emission spectroscopy (XPS) measurements, see figure 4.2. The aluminum was oxidized in air and by 60s of oxygen plasma etching. On top of the electrodes about 70 nm of pentacene was deposited in UHV with a base pressure $\leq 5{\cdot}10^{-10}$ mbar. Figure 4.3 shows a typical AFM image of a pentacene layer of 85 nm and shows grain sizes of about 1 μm. Pentacene was obtained from Sigma-Aldrich and purified twice by vacuum sublimation and stored under N_2 atmosphere before it was loaded in UHV. After deposition of pentacene, the samples were taken into air, glued to a 24-pins sample holder and bonded. Exposure to air after pentacene deposition was minimized by storing the samples in a small vacuum chamber (p $\approx 10^{-1}$ mbar) with P_2O_5 powder to extract water.

Figure 4.4 shows the current-voltage characteristics for cobalt, gold and cobalt/aluminum oxide finger electrodes as measured at room temperature in a small vacuum chamber, which was continuously pumped by a turbo molecular pump (p $\approx 5{\cdot}10^{-6}$ mbar). We used a Keithley 6517 electrometer as voltage source and current meter. The delay time between two points was about 0.1 s and ramping of the voltage was done slowly, ≤ 1 V/s. The measurements for cobalt and gold electrodes have been reproduced in a second sample of the same batch within an accuracy of 15 %. The cobalt/aluminum oxide samples showed less reproducibility, hence two typical samples are displayed in figure 4.4.

The data in figure 4.4a) is given as current density versus electric field. For the current density we

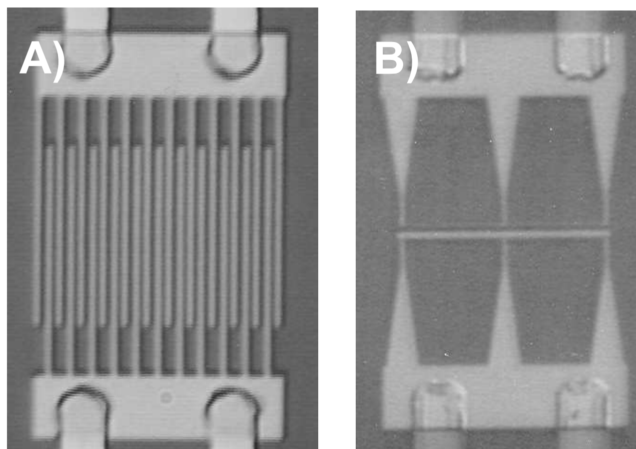

Figure 4.1: A) Optical microscope image of the 'finger' electrode pattern. Effectively, 22 pairs of electrodes are present with a width of 300 nm, a spacing of 300 nm and an effective length of 10 μm. B) Optical microscope picture of the 'bar' shaped electrodes. Both electrodes have a width of 14 μm, the widths are 300 nm and 100nm, for the lower and upper electrode and they are separated by 300nm .

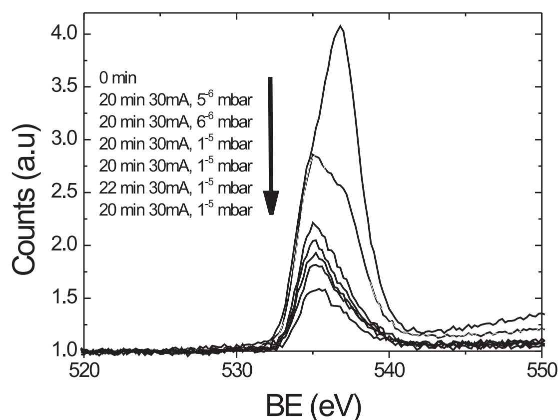

Figure 4.2: XPS spectra of a cobalt surface with a native oxide layer during argon milling. The spectrum shows the number of electrons versus the energy of electrons emitted from the surface. The peak at 537 eV is 1S peak of oxygen. The argon milling time and argon pressure and ion current are given for each spectrum. The ratio between the peak surfaces of the first and last peak is about 5:1, indicating that 4/5 of the oxide layer is removed. Argon milling usually does not remove all oxide, since some oxygen atoms will be 'pushed' into the cobalt by the argon ions.

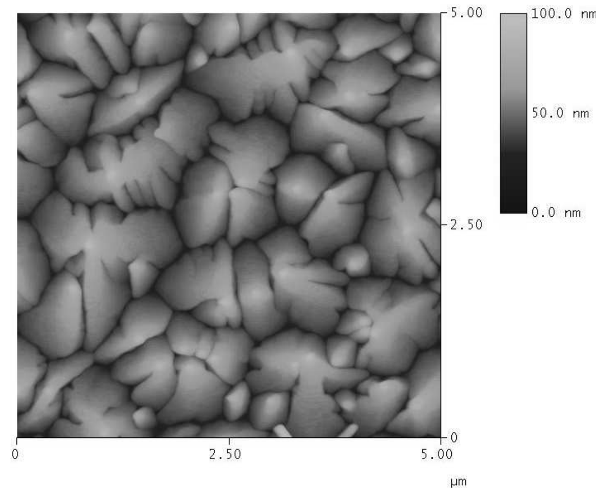

Figure 4.3: Typical AFM picture of a 5 x 5 μm^2, 85 nm thick pentacene film on silicon oxide. Pentacene shows irregularly shaped grains with a typical size of about 1 μm.

Table 4.1: Mobility (μ), carrier density (n) and onset field (E_0) determined using the SCLC model.

Electrode material	μ ($10^{-2} cm^2/Vs$)	n (10^{15} cm^{-3})	E_o (10^6 V/m)
gold	2.2	2.6	4.5
cobalt	3.2	6.4	10

assumed that conduction is through the entire layer (about 70nm) along the full width ($22 \cdot 10$ μm) of the electrodes. SEM pictures of the finger pattern before deposition of pentacene showed there is a spread in l within the finger pattern of about 10 %. The samples were also measured at negative bias such as given in figure 4.4b-e. The gold and cobalt samples mostly showed symmetric behavior, *eg* I(V)=-I(-V). The cobalt/aluminum oxide samples showed both symmetric and asymmetric behavior, such as displayed in figure 4.4d-e. No hysteresis was observed below a pressure of 10^{-4} mbar. Cobalt/aluminum oxide samples show a quadratic dependence on voltage at electric fields between 10^5-10^8 V/m. Also, the resistances for these samples (typically 1 GΩ at 5V) are much higher than the clean contact samples (typically 1-10 MΩ at 5V).

For cobalt and gold, both measurements globally show the same characteristics. A typical resistance for cobalt samples is 1 MΩ at 5V. A typical resistance for the gold samples is 10 MΩ at 5 V. At low electric fields linear behavior is observed, whereas at higher fields a stronger dependence on voltage is observed. We quantify the transition between these two regions, by taking the electric field value for the crossing point, E_o, of a linear fit of the low field part and quadratic fit of the high field part. By assuming SCLC one can abstract the mobility as described in section 2.2.2 and by assuming that Θ=1 and ϵ_r =3 [21]. Also, if one assumes drift only in the linear part, the current density is given by:

$$J = e\mu nE$$

Here, e is the electronic charge, E the electric field and n the number of charge carriers. If we extract μ from the high field part, we can extract the number of charge carriers from the linear part. The results, an average of two samples, are given in table 4.1. The values of μ are in reasonable agreement with values of μ reported elsewhere (see appendix C).

4.3 Temperature dependence

To investigate the temperature dependence of charge transport we used two experimental approaches to measure samples with patterned gold electrodes. Firstly, we loaded the samples previously measured in the small vacuum chamber at room temperature in a dip-stick (10^{-5} mbar), which can be held in

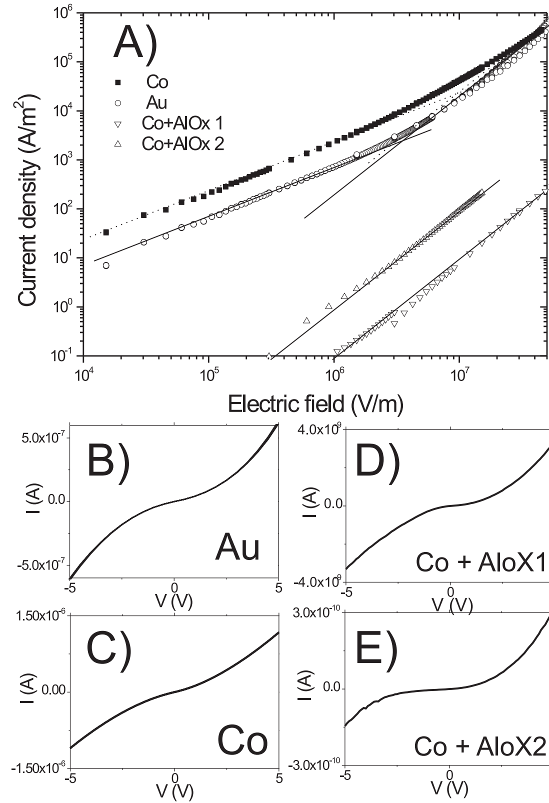

Figure 4.4: Current voltage characteristics for finger patterns with 5 nm Ti/25 nm gold, 25 nm cobalt and 10 nm cobalt/aluminum oxide electrodes. A) Log-log plot of current density versus electric field for finger electrodes with a 300 nm separation of cobalt and gold. At fields up to 10^6 V/m cobalt and gold electrodes show linear behavior. At higher fields a stronger dependence on voltage is seen. For cobalt/aluminum oxide electrodes a quadratic dependence on voltage is obtained. The lines are guides for the eye and are linearly (for cobalt and gold at low fields) or quadratically dependent on voltage. Data points are recorded with several different range settings of the electrometer. The discontinuity in the data points of cobalt/aluminum oxide might be caused by partial breakdown of the sample. B-E) Current-voltage characteristics between -5 and 5 V for the same samples as shown in A). B) and C) are typical results for cobalt and gold, respectively. D) and E) are two typical samples for cobalt/aluminum oxide electrodes. Reproducibility for cobalt/aluminum oxide was more difficult than for cobalt and gold. All given results were measured at room temperature and p $\approx 5{\cdot}10^{-6}$ mbar.

a vessel of liquid nitrogen (77 K) and connected to an electrometer. Cooling down in this way will further reduce pressure in the vacuum chamber due to cryogenic pumping of the walls of the vacuum chamber. For a second approach we adjusted a chamber in UHV and built a sample holder which could be cooled by liquid nitrogen and heated by sending current through high resistive wires. Two pins (made of household sewing needles), which position was manipulated by screws outside the vacuum, connected the electrometer with the sample. In order to contact the pins, large contact pads (0.5 mm^2) were made by electron beam lithography in order to contact the needles with the patterned electrodes. We used a camera, which was placed outside UHV above a window in the chamber to magnify the contact pads.

Current voltage characteristics were obtained in the same way as described above. For the measurements in UHV we used the finger pattern with a spacing of 600 nm between the electrodes. For the dip-stick measurements we used the bar pattern, such as given in figure 4.1b. Figure 4.5a shows current density versus electric field as a function of temperature for the measurements in UHV. Clearly, the resistance of the samples increases with decreasing temperature. Also, the current density at room temperature in UHV is lower compared to measurements at $p = 10^{-6}$ mbar, see figure 4.4. Cooling increases the resistance and at low temperature we observe an exponential voltage dependence. Note that the characteristics at 300K did not fully recover after one cycle of cooling and heating and also not after a second cycle of heating (400K) and cooling, indicating that permanent changes occurred during the measurements. Remarkably, the characteristics at room temperature after cooling and heating show a clear exponential voltage dependence at high fields, whereas before cooling and heating this dependence was much weaker.

The measurement in the dipstick are shown in figure 4.5b and qualitatively show similar behavior. Again an exponential current dependence on voltage is observed at low temperatures, which is made even more explicit in the inset, see figure 4.5c. However, current densities were higher compared to measurements in UHV and current voltage characteristics recovered after one cycle of cooling and heating (77K-300K).

We also observed the following general behavior. At high voltages ($\geq$50V) current started to increase dramatically (up to several mA) and strong hysteresis appeared. When measuring pentacene in UHV in the presence of white light (bright spot) current increased by a factor of 2-4. Allowing ambient air into a vacuum chamber while measuring, strongly (factor of 10) decreased the resistance at low voltages. Also, IV-characteristics fully recovered after one cycle of venting and pumping in the dip-stick.

4.4 Discussion

Cobalt and gold are similar electrode materials, since their work functions (5.4 and 5.0 eV) are quite alike. Still we observe a 10 times higher resistance in the linear part of gold compared to the linear part of cobalt. Also, the trend in, and magnitude of the hole injection barriers for cobalt (1.05 eV) and gold (0.85 eV), predicted by our simple model in figure 2.10, is not clearly reflected in the data of figure 4.4a and by the values of E_0.

Cobalt/aluminum oxide samples show a quadratic dependence on voltage. This agrees with the SCLC model. The resistances in samples with cobalt/aluminum oxide electrodes are much higher (typically 1 GΩ at 5V) than resistances in samples with cobalt or gold electrodes (typically 1-10 MΩ at 5V). One would expect that tunneling through the barriers is the limiting factor. This yields an exponential voltage dependence of the current, which would not give a straight line in figure 4.4a. Another possibility is that the charge transport with clean contacts is being dominated by a mechanism which is not present when introducing tunnel barriers. So far, the issue remains unresolved.

Below $p=10^{-6}$ mbar, resistance of the pentacene thin layers continues to increase. However, in single crystals resistance saturates at pressures of 10^{-6} mbar [22]. The increase of current upon exposure into air has been previously attributed to oxygen [24]. Oxygen easily penetrates pentacene and in thin films this effect might be more pronounced, even at pressures $p < 10^{-6}$ mbar.

We observe a linear regime up to electric fields of 10^6 V/m in the current voltage characteristics at room temperature for cobalt and gold electrodes. A possible explanation for this linear regime

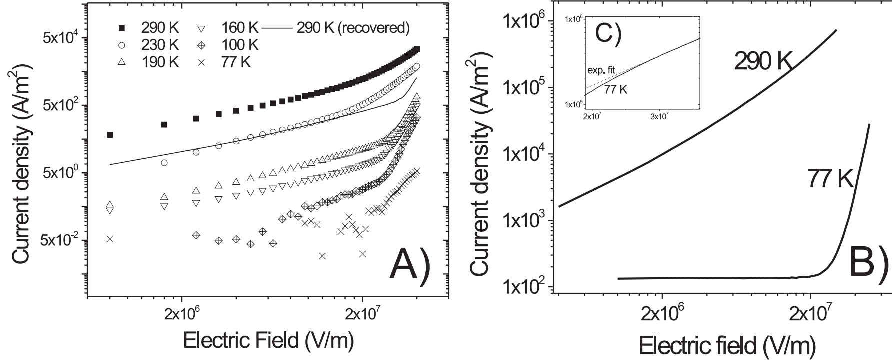

Figure 4.5: Temperature dependence of charge transport in pentacene thin-films. A) Log-log plot of current density versus electric field for finger electrodes of gold with l = 300 nm as a function of temperature measured in UHV. The spread in points at very low current densities is due to limitations in the resolution of the electrometer. Note that the current-voltage characteristic is not reproduced after one cycle of cooling and heating (solid line). B) Log-log plot of current density versus electric field for measurements at room temperature and liquid nitrogen temperature in a dip-stick. NB: this sample only has 2 electrodes (14 x 0.300 μm^2) of gold with l = 300 nm. The flat line at 77K at low fields represents the lower limit of the electrometer. C) At 77K at high fields the current density is exponentially dependent on the electric field as is shown by the linear fit in a plot of current density on a logarithmic scale versus electric field on a linear scale.

is metal-like conduction through trap states of thermally generated carriers. The trap states can be created by impurities, causing levels in the band-gap. Electrons and holes in these states can be thermally activated ($n=10^{15}$ cm^{-3}) if they are within an energy ($\approx k_bT$) of the Fermi level. The strong reduction of current at lower temperatures supports this hypothesis.

Our results showed a suppression and an exponential voltage dependence of the current at lower temperatures. To the best of our knowledge, from literature, it is not exactly clear what to expect. For example, the temperature dependence of hole mobility in pentacene single crystals showed a slight increase in mobility (which is proportional to the current), while lowering temperature [22]. In thin films the usual trend is a diminishing hole mobility, while lowering the temperature [30] [28].

In our case, the suppression of the linear part at low temperatures matches the thermal activated trap picture. At higher fields at low temperatures the current depends exponentially on voltage. Exponential dependence is usually associated with tunneling. Figure 4.6 gives a possible explanation for this observation when considering the whole device in a simple insulator band picture. At biases higher than the band gap, holes and electrons can tunnel directly through the gap into the valence and conduction band, respectively. In principle this is independent of temperature. However, the exponential behavior might be less clearly seen at higher temperatures, when the conduction via (impurity) states in the band gap dominates charge transport. Exponential increase of the current with voltage is also reported for ambipolar pentacene thin film transistors [33] [32], which supports this hypothesis.

4.5 Conclusions

We investigated charge transport in pentacene thin-films with lateral electrode patterns. We observed that the resistance of pentacene thin films increases with decreasing temperature and decreasing pressure. At room temperature charge transport with clean contacts can be described by a linear current-voltage dependence up to fields of 10^6 V/m, which might be caused by thermally activated carriers from impurity states in the band gap. The strong increase in resistance of the linear regime supports this explanation. At higher fields, the current increases faster than linearly with voltage.

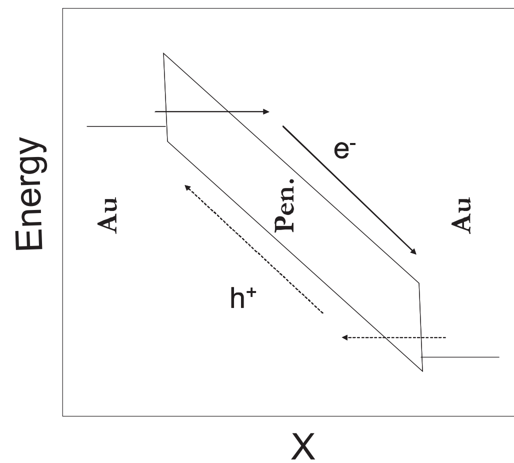

Figure 4.6: Possible explanation for exponential voltage dependence of pentacene at high biases when modeling pentacene in a simplified band picture. An energy diagram for pentacene connected to gold is given under high bias. At high biases holes and electrons can tunnel through the energy gap directly into the valence band. The barrier for electrons is higher than for holes, since the Fermi level of gold is closer to the valence band of pentacene than to the conduction band.

Assuming SCLC, hole mobilities of 0.02-0.03 cm^2/Vs can be extracted. At lower temperatures, a clear exponential voltage dependence of current is observed, which can be explained by through band gap tunneling of holes in the valence band. When introducing tunnel barriers in between the cobalt electrodes and pentacene we observed a quadratic voltage dependence at electric fields of 10^5-10^8 V/m.

Chapter 5

Towards spin injection: a non-local measurement

5.1 Introduction

A few attempts to measure the magnetoresistance of spin injection devices with pentacene have been performed. Both 2 probe DC measurement and 4 probe non-local measurements with lock-in techniques have been carried out. So far, these measurements showed no magnetoresistance. To illustrate problems encountered, in this chapter we show data of a device with clean contacts. We did not choose a sample with tunnel barriers, since these samples give higher resistances than our lock-in measurement equipment is able to measure.[1] Although we expect the conductivity mismatch problem to be present in this case, measurements on samples with clean contacts can check the level of the background resistance and noise levels.

5.2 A first attempt: a non-local measurement

In order to determine the possibility of 4-probe measurements, several samples with four adjacent rectangular shaped cobalt electrodes were fabricated. The samples were prepared similarly to the samples described in chapter 4. A SEM picture of the electrodes is given is given in figure 5.1. The electrodes are 25 nm thick and the spacing between subsequent electrodes is 100 nm. Magnetization of the inner electrodes can be reversed independently from to the magnetization of the outer two by applying a magnetic field. The widths of the electrodes are 130nm and 400nm, corresponding to switching fields of about 50 mT and 10 mT, respectively. Cobalt oxide was removed by argon milling and after pentacene deposition, samples were bonded and loaded in a vacuum chamber with $p = 10^{-6}$ mbar, which was placed between magnetic coils. The pattern was tested by performing DC 2-probe measurements for each combination of electrodes.

An oscillating voltage signal (frequency = 2 Hz) was fed to a current source (IV-Meetkast), which produced an oscillating current. This signal was sent through the bottom two electrodes in figure 5.1 at two different DC biases (0 A bias, 0.1 μA oscillation and 0.4 μA bias, 0.01 μA oscillation). The voltage drop over the upper two electrodes was measured by using a lock-in amplifier and a voltage amplifier (IV-meetkast). Resistance was determined as a function of magnetic field applied parallel to the long axis of the strips. Results are shown in figure 5.2. Time between measuring points is 16 seconds and the lock-in time constant is 3 s. No switching is observed and non-local resistances are in the same order of magnitude as local resistances (10 MΩ). The noise level is about 1 % of the background signal. We were expecting a background resistance in non-local geometry close to 0 ohms. The observed large background signal is worrying and reproducibility of this experiment should be checked.

[1] Recent improvements on our equipment (IV-meetkast) have solved these problems and lock-in measurements on samples up to TΩs are possible now.

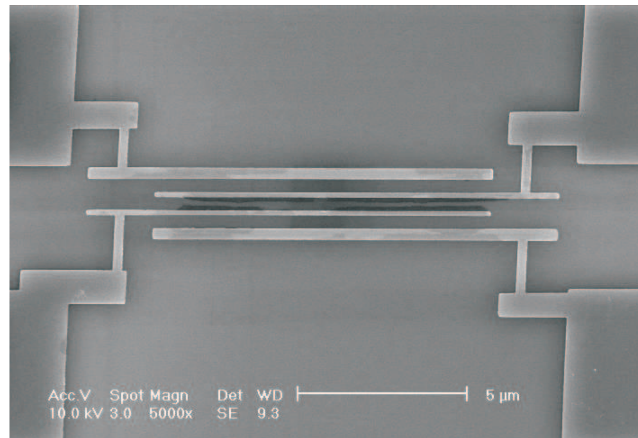

Figure 5.1: SEM picture of cobalt electrodes used for 4-probe measurements. Subsequent electrodes in this sample have a spacing of 420 nm. Note that the results of the sample discussed above have a spacing of 100 nm. The widths of the electrodes are 130 nm and 400 nm, respectively. This allowed independent switching of the two inner electrodes as compared to the outer two.

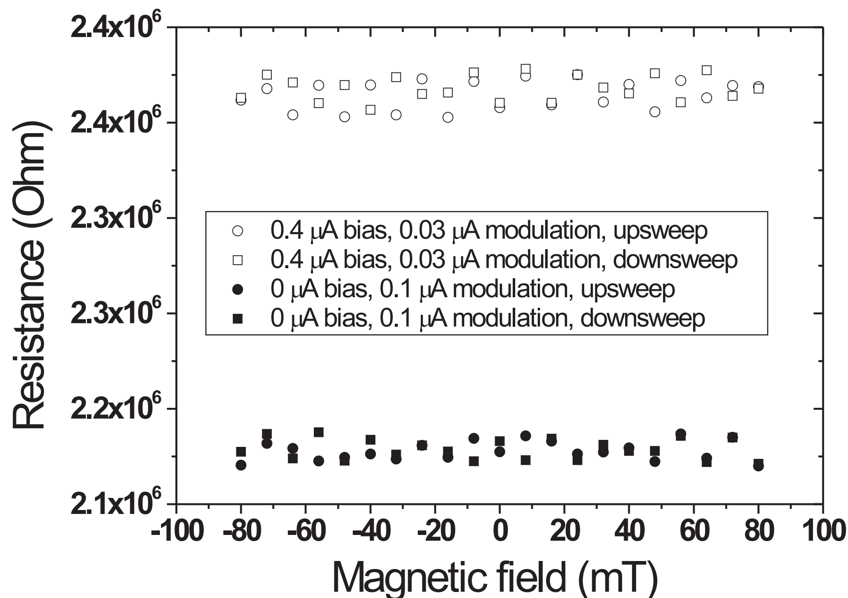

Figure 5.2: Non-local resistance of pentacene as a function of increasing magnetic field (circles) and decreasing magnetic field (squares) at room temperature, p $\approx 5{\cdot}10^{-6}$ mbar and at two different biases. The geometry is comparable to the one given in figure 2.7. The current was sent through the bottom two electrodes and voltage was measured between the two upper electrodes in figure 5.1.

5.3 Conclusions

In a single, first attempt to measure a non-local spin injection signal with clean contacts no magnetoresistance was observed. The background signal (2 MΩ) is in the order of the 2-probe resistance (10 MOhm). Reproducibility of these measurements should be checked. The noise level observed in these measurements is about 1 % of the background signal.

Chapter 6

Conclusions

6.1 Conclusions

Several experiments on the road to spin injection in organic materials exploring the fabrication of magnetic tunnel junctions, the charge transport in pentacene thin layers, and the possibility of measuring in a 4-probe non-local geometry have been reported. No spin-injection has been observed so far. The main conclusions of these experiments are listed below.

By oxidizing cobalt/aluminum heterostructures in air, and applying a semiconductor on top, FSTJs can be obtained. After oxidation in air, closed oxide layers are formed on top of heterostructures of 9/10 nm cobalt and 2 nm aluminum. AMR measurements showed that switching field of magnetization reversal in rectangular cobalt strips with a height of 9 nm can be controlled by an external magnetic field by changing the width of the strips. The relative value of the AMR when switching the magnetization by a magnetic field applied perpendicular to the long axis of the strip was found to be 0.3 %. Switching fields of 8-17 mT were found for strips with a widths of 1640-240 nm when reversing the magnetization along the long axis of the strips. The control of oxidation cobalt/aluminum heterostructures in air is limited and yield barriers with a typical resistance of GΩs.

Charge transport measurements of pentacene thin-films with lateral electrode patterns showed that the resistance of pentacene thin films increases with decreasing temperature and decreasing pressure. At room temperature charge transport with clean contacts can be described by a linear current-voltage dependence up to fields of 10^6 V/m, which might be caused by thermally activated carriers from impurity states in the band gap. At higher fields, the current increases faster than linearly with voltage. Assuming SCLC, hole mobilities of 0.02-0.03 cm^2/Vs can be extracted. At lower temperatures, a clear exponential voltage dependence of current is observed. When introducing tunnel barriers in between the cobalt electrodes and pentacene we observed a quadratic voltage dependence at electric fields of 10^5-10^8 V/m.

In a single, first attempt to measure a non-local spin injection signal with clean contacts no magnetoresistance was observed. The background signal (2 MΩ) is in the order of the 2-probe resistance (10 MΩ). Reproducibility of these measurements should be checked. The noise level observed in these measurements is about 1 % of the background signal.

6.2 Prospects

For organic systems the conductivity mismatch is a fundamental problem. Interface barriers might be a solution. Thin aluminum oxide barriers seem a suitable candidate. Attempts to make these barriers in spin injection devices yielded barriers with a resistance of about 1000 times the resistance of pentacene itself. On the basis of a simple model, see section 2, we do not expect any magnetoresistance for these barriers. The thickness of the barrier should be reduced below the native oxide thickness of aluminum. This requires a controlled and clean oxygen environment. Aluminum evaporation and controlled oxidation in UHV seem the best candidate for producing these barriers. One should also be careful for oxidation of the underlying cobalt after fabrication of ultrathin aluminum oxide barriers. Therefore completely working and measuring in UHV or protecting samples against air seems

necessary. Measuring and processing completely in-situ requires shadow mask techniques for multiple evaporation steps (or physical masks for big patterns) and the presence of a measurement setup in UHV with a magnet. Especially this last demand requires quite some (time) investments.

The results so far did not clearly show SCLC. Therefore, the obtained mobilities and charge carrier densities are ambiguous. To obtain charge transport parameters more properly one can use the field effect transistor geometry using SiO_2 as a gate dielectric. The enhancement of the number of charge carriers by electrical doping will probably also be beneficial for spin transport, since the number of spins will also increase. Still, the discrepancy between charge transport measurements in thin films and single crystals is striking. The most straightforward explanation for this discrepancy is the structural disorder in pentacene thin films. A further exploration of the influence of structural disorder on charge transport is needed to account for the charge transport mechanism in pentacene thin films.

Non-local background resistances unequal to zero are worrisome. Electrode spacing dependence of non-local resistance of locally deposited pentacene is the most straightforward step exploring this problem. If this problem cannot be solved, a solid proof of spin-injection seems cumbersome.

Appendix A

RESISTOR MODEL WITH R_{REL}

The model given in figure 2.5 can be generalized and subsequently simplified as given in figure A.1. Here, we make use of the so called Kennely star-delta transformation [46] in which the star of R_1, R_2 and R_5 is replaced by a delta, with resistances as given in the figure.
The resistance of the two resistors in parallel in the lower left part of the diagram is given by

$$Z_{left} = 1/(1/R4 + 1/(R1 + R2 + R1R2/R5))$$

The resistance of the two resistors in parallel in the lower right part of the diagram is given by

$$Z_{right} = 1/(1/R3 + 1/(R2 + R5 + R2R5/R1))$$

The total resistance across the network is calculated as:

$$\frac{1}{(1/Z_{top} + 1/(Z_{left} + Z_{right}))}$$

$$\frac{1}{\frac{1}{(R1+R5+R1R5/R2)} + \frac{1}{\frac{1}{R4}+\frac{1}{R1+R2+R1R2/R5}} + \frac{1}{\frac{1}{R3}+\frac{1}{R2+R5+R2R5/R1}}}$$

This expression can be simplified as:

$$\frac{R1R2R3 + R4R2R5 + R1R2R4 + R3R2R5 + R1R3R4 + R5R3R4 + R3R1R5 + R4R1R5}{R4R5 + R1R3 + R1R5 + R3R4 + R5R2 + R1R2 + R4R2 + R3R2}$$

In our case, R1-R5 in the parallel and the anti-parallel configuration of figure 2.5 are given by:
parallel

$$R1 = R5 = R_{TB\uparrow\uparrow} + 1/2R_{SC} = \frac{R_{TB}}{1-P} + 1/2R_{SC}$$

$$R2 = R_{REL}$$

$$R3 = R4 = R_{TB\uparrow\downarrow} + 1/2R_{SC} = \frac{R_{TB}}{1+P} + 1/2R_{SC}$$

anti-parallel

$$R1 = R3 = R_{TB\uparrow\uparrow} + 1/2R_{SC} = \frac{R_{TB}}{1-P} + 1/2R_{SC}$$

$$R2 = R_{REL}$$

$$R4 = R5 = R_{TB\uparrow\downarrow} + 1/2R_{SC} = \frac{R_{TB}}{1+P} + 1/2R_{SC}$$

The parallel resistance, R_P, is now given by:

$$1/2(2R_{TB} + R_{SC} + R_{SC}P)\frac{2R_{TB} + R_{SC} - R_{SC}P}{2R_{TB} + R_{SC} - R_{SC}P^2}$$

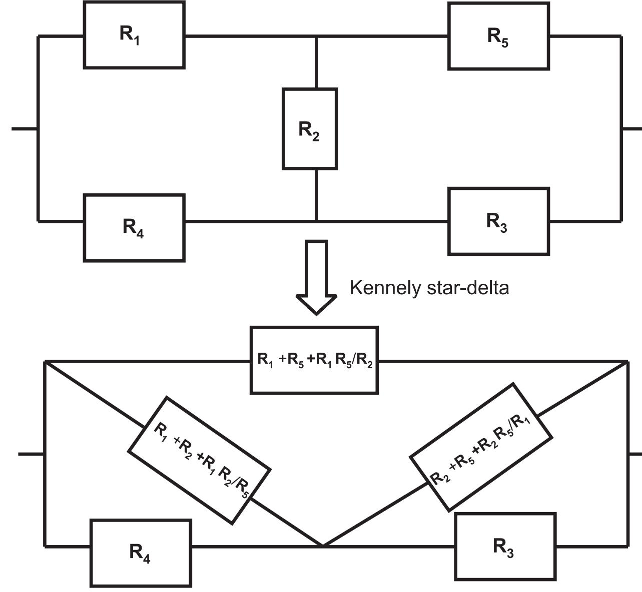

Figure A.1: Simplified picture of the resistor network. A Kennely star-delta transformation can be used to calculate the overall resistance of the network.

The anti-parallel resistance, R_{AP} is given by:

$$1/2\frac{(4R_{REL}R_{TB} + 2R_{REL}R_{SC} - 2R_{REL}R_{SC}P^2 + 4R_{TB}^2 + 4R_{TB}R_{SC} + R_{SC}^2 - R_{sc}^2P^2)}{2R_{TB} + R_{SC} - R_{SC}P^2 + 2R_{rel} - 2R_{REL}P^2}$$

NB: The resistance in the parallel configuration is not dependent on R_{REL}.
Subtracting R_{AP}-R_P and dividing by R_P, yields equation 2.1.

To relate R_{REL} to the spin flip length we assumed the following. We can describe the semiconductor as given in figure A.2. We consider the two spin channels, with chemical potentials μ_0 for the spin up channel and $-\mu_0$ for the spin down channel. We assume an exponential decay/increase [12] for the spin up /spin down channel and the chemical potentials halfway between the electrodes, L/2 and L such as given in figure A.2. Now we consider the currents I_1 and I_2. I_1 is given by:

$$I_1 = \frac{\mu_0(1 - exp(\frac{L}{2\lambda_{sf}}))}{eR}$$

Where e is the electron charge. I_2 is given by:

$$I_2 = \frac{\mu_0(exp(\frac{-L}{2\lambda_{sf}}) - exp(\frac{-L}{\lambda_{sf}}))}{eR}$$

Now we can calculate i, since Kirchoff rules state that:

$$\begin{aligned} i = I_1 - I_2 &= \frac{\mu_0}{eR}(1 - 2exp(\frac{-L}{2\lambda_{sf}}) + exp(\frac{-L}{\lambda_{sf}})) \\ &= \frac{\mu_0}{eR}(1 - exp(\frac{-L}{2\lambda_{sf}}))^2 \end{aligned}$$

Now, R_{REL} is given by the difference in chemical potentials at both sides of R_{REL} divided by i:

$$\begin{aligned} R_{rel} &= \frac{2\frac{\mu_0}{e}exp(\frac{-L}{2\lambda_{sf}})}{\frac{\mu_0}{eR}(1 - exp(\frac{-L}{2\lambda_{sf}}))^2} \\ &= \frac{2Rexp(\frac{-L}{2\lambda_{sf}})}{(1 - exp(\frac{-L}{2\lambda_{sf}})^2)} \end{aligned}$$

In our case, R=1/2R_{SC} which gives equation 2.2.

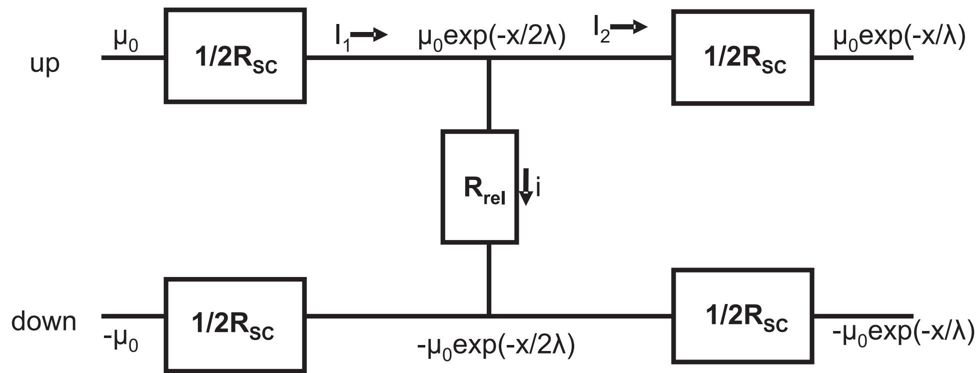

Figure A.2: Schematic representation of the semiconductor. We assume a chemical potential μ_0 for the spin up channel and a chemical potential -μ_0 for the spin down channel and a exponential decay of the chemical potential with distance from the interface, L.

Appendix B

DERIVATION SPACE CHARGE LIMITED CURRENT

We start from the following:

1. The current is given by
$$J = en(x)\mu E(x) \ or \ E(x) = \frac{J}{en(x)\mu}$$
eg. We assume drift and neglect diffusion.

2. The number of charge carriers is given by Poisson's equation[1]:
$$n(x) = \frac{\epsilon}{e}\frac{dE(x)}{dx}$$

3. We assume Ohmic contacts,
$$E(0) = 0$$

4. The total voltage across the insulator is given by:
$$V = \int E(x)dx$$

Substituting 2 into 1 we obtain:
$$E(x) = \frac{J}{\mu\epsilon}\frac{dx}{dE(x)}$$
Here $E(x) = 1/2\frac{d(E^2)}{dE(x)}$, so
$$1/2d(E^2) = \frac{J}{\mu\epsilon}dx$$
Integration over E^2 and x gives:
$$1/2E^2 = \frac{J}{\mu\epsilon}x + C$$
When neglecting the constant
$$E(x) = \sqrt{\frac{2J}{\mu\epsilon}x}$$
When using 4 and integrating from x=0 to x=L while using 3 we obtain:

[1]Note that if we use the number of charge carriers present on the sides of a parallel plate capacitor for n(x), $n = CV = \epsilon\epsilon_0 V/L$, we already obtain child's law, with a factor of 8/9 missing.

$$V = \sqrt{\frac{2J}{\mu\epsilon}} \int_0^L \sqrt{x} = \sqrt{\frac{2J}{\mu\epsilon}} 2/3 L^(3/2)$$

Which eventually gives Child's law:

$$J = \frac{9}{8} \mu\epsilon \frac{V^2}{L^3}$$

Appendix C

PROPERTIES OF PENTACENE

Table C.1: Properties of pentacene

Melting point	270°
Density	278.33 g mol^{-1}
Formula	$C_{22}H_{14}$
Color	Violet
Resistivity	10^5-$10^8\Omega$ m depending on crystal direction
Crystal system	Triclinic

Table C.2: Mobilities of pentacene in hole only injection devices

Source	μ (RT) (cm^2/Vs)	**C**rystal/**F**ilm	method[1]	T depend.[2]	spacing (l)	Contacts[3]
[22]	10-50	C	SCLC	-	mm	T
[30]	2	F	TFT	+	μm	T
[23]	0.024	F	TFT	?	μm/nm	B
[47]	0.9	F	TFT	?	100μm	B
[28]	1	F(single grain)	TFT	+	40μm	T
[48]	1.4	C	Flip	?	mm	B

[1] *TFT = thin film transistor, SC = space charge limited current, flip = flip crystal method*
[2] *-=increase in μ with decreasing temperature*
[3] *T=top, B=Bottom*

Appendix D

PROCESS DETAILS

D.1 General recipe

1. Optical Lithography
    - cleaning of 2” wafer silicon quest international, Boron doped, 1-10 Ωcm (500 nm SiO_2)
        - boil in acetone (5 min)
        - ultrasonic
        - rinse in IPA and ethanol for 5 min
        - spin dry
        - oven (170°C, 3min)
    - Resist spinning
        - LOR 3A (5000 RPM, 60 s)
        - oven (190°C, 5 min)
        - s1813 (5000 RPM, 60 s)
        - oven (115°C, 2 min)
    - Exposure
        - new mask 7B, align and clamp
        - expose (2s)
        - clean Mask in PRS3000
    - Development,**sensitive!**
        - CD-26 (20s)
        - water (10s)
        - spin dry
        - oven (125°C, 5 min)
        - CD-26 (10s)
        - water (10s)
        - spin dry
        - O_2 RIE (10s, 40W 9 μbar 0.9 sccm)
        - check by optical microscope
    - Deposition
        - 5 nm Ti (p=5 10^{-7}mbar, 0.15nm/s
        - 25 nm Au (p=5 10^{-7}mbar, 0.20nm/s)
    - Lift off
        - PRS300 (overnight)
        - ultrasonic (30 s)

  - rinse in water
  - spin dry

2. Electron beam lithography

- Cutting and spinning
  - cut wafer in 3x3 samples
  - blow dry with N_2
  - rinse in acetone
  - ultrasonic (3 samples, 2 min)
  - rinse in ethanol
  - ultrasonic (3 samples, 1 min)
  - spin dry
  - O_2 RIE (1 min, 40W, 9 μbar 0.9 sccm)
  - check by optical microscope
- spinning
  - PMMA 2010 in Cl-benzene (3000 rpm 60s)
  - oven (150°C, 15 min)
  - PMMA 2041 in O-xylene (4000 rpm 60s)
  - oven (150°C, 15 min)
- electron beam lithography (41.9 pA 800x dose 2.5, for high currents for PADS UHV: 5 nA)
- development
  - IPA:MIBK 3:1 (60s)
  - IPA 60s
  - spin dry
  - O_2 RIE (10 s, 40W, p=9 μbar 0.9 sccm)
  - check by optical microscope

3. Deposition

- Temescal: 5 nm Ti (p=5 10^{-7}mbar, 0.15nm/s)
- Temescal: 25 nm Au (p=5 10^{-7}mbar, 0.20nm/s)
  or
- Temescal: 25 nm Co (p=5 10^{-7}mbar, 0.20nm/s)
  or
- Temescal: 9 nm Co (p=5 10^{-7}mbar, 0.20nm/s)
- Temescal: 1.8-2.0 nm Al (p=5 10^{-7}mbar, 0.20nm/s)

4. Lift off

- hot acetone (2 hours)
- ultrasonic (30s)
- acetone syringe squeezing
- ethanol rinse
- ethanol syringe squeezing
- spin dry
- oven (150°C, 3 min)
- O_2 RIE (1 min, 40W, 9 μbar 0.9 sccm)

5. Resist window (optional)
   - spinning
     - PMMA 2010 in cl-benzene (3000 rpm 60s)
     - oven (150°C, 15 min)
     - PMMA 2041 in xylene (4000 rpm 60s)
     - oven (150CC, 15 min)
   - electron beam lithography (41.9 pA 800X dose 2.5, for high currents for PADS UHV: 5 nA,)
   - development
     - IPA:MIBK 3:1 (60s)
     - IPA 60s
     - spin dry
     - O_2 RIE (10 s, 40W, p=9 μbar 0.9 sccm)
     - check by optical microscope
6. Pentacene deposition
   - mount sample and blow with N_2
   - load sample in UHV
   - argon ion cleaning Au/AlO (10 min) Co (60 min) (p=1 10^{-5}mbar, emission current = 13 mA, Acc V = 1.5 kV)
   - pentacene deposition (200°C, 0.02-0.06nm/min, 125 min)
7. Bonding (not in UHV)
   - remove from UHV
   - glue sample on 24-pins chip carrier
   - put in vacuum chamber with P_2O_5 and pump for 1 hour
   - bond in air
   - put in dipstick or vacuum chamber and pump

D.2 Chemicals

Table D.1: Industrial resists (r) and resit removers (rm)

Name	company	use
Lor-3A	MicroChem	r
S1813	Shipley	r
PRS 3000	JT Baker	rm

D.3 Processing machines

Processing was mainly done in the clean room of the Physics of Nanodevices group. Pentacene deposition and XPS/UPS analysis was done in a UHV system of H.T Jonkman, (Bio)organic Materials and Devices group. The clean room facilities of the Physics of Organic Semiconductors (RuG/MSC) were used for the deposition of aluminum during the breakdown experiments.

Table D.2: Processing machines

system	company	additional information
EBL	JEOL	JSM-840 with Raith Elphy software
Optical lithography	Karl Suiss	MJB 3
Metal deposition	Airco-Temescal	2 kW e-gun evaporator
Metal deposition	Paul Blom	
Sputtering	Leybold Heraeus	Z 400
RIE	Home build	-
XPS/UPS	-	-
AFM	Digital instruments	Multi mode SPM
SEM	Philips	-
Surface profiler	Dektak	-
Bonding	Home build	-

Appendix E

MEASUREMENT DETAILS

Table E.1: Analysis instruments

Instrument	Details
Lock in Amplifier (2x)	Stanford Research systems
IV-meetkast	home build
Multimeter	Prema 5000
DC voltage source	Keithley 220
DC current source	Keithley 230
Electrometer	Keithley 6517
Magnet current source	Electronic meas. inc. BOSS
Magnet	GMW 3470 electromagnet

Appendix F

EXTRA: AN ALUMINUM OXIDE GATE

In order to investigate the quality of an AlO_x layer we determined the breakdown voltage of an aluminum/AlO_x/gold heterostructure. Patterns were made by electron beam lithography. A bar of 35 nm thick aluminum was deposited thermally in vacuum (p=10^-7mbar) in a system which was placed in a N_2 glove box. The aluminum was oxidized in air and by 60s of oxygen plasma etching. The roughness of the surface was determined by AFM to be 1.0 nm RMS. On top of the Al bars 8 chromium/gold (3nm and 70 nm) contacts were deposited, yielding four contacts with a contact surface of 0.3 μm^2 and four contacts with a contact surface of 0.6 μm^2. Structures were made similar as described in the general recipe D. An optical microscope photograph of a device is given in figure F.1.

The breakdown was measured by slowly increasing the voltage with a Keithley 230 voltage source, while measuring the current with a Keithley 6517 electrometer. Up to the breakdown voltage a current of several picoamperes can be measured. Current voltage characteristics after breakdown were linear with a typical resistance of 800 Ω. The breakdown voltages for different devices are given in figure F.2. The spread in breakdown is quite high, indicating bad oxide quality. However, if we assume a native oxide thickness of 3 nm, 7 volts breakdown corresponds to an electric field of 2.3 GV/m.

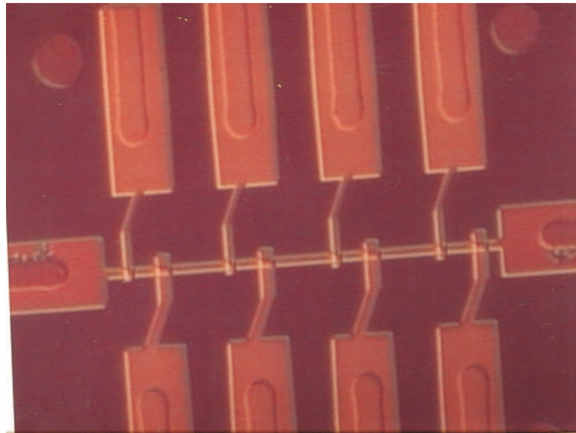

Figure F.1: Optical microscope photograph of a aluminum bar oxidized in air contacted to two bottom electrodes and 8 gold top electrodes in order to determine the breakdown voltage of a native AlO_x layer. The length of the aluminum bar is approximately 35 μm.

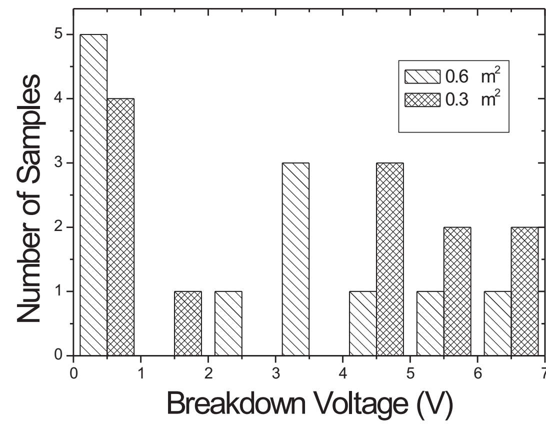

Figure F.2: Histogram of the breakdown voltage of 24 samples with aluminum/AlO_x/gold heterostructure to determine the quality of the AlO_x layer.

Bibliography

[1] G. J. Stoney. *Of the electron or atom of electricity*. Philosophical Magazine **38**, 418 (1894).

[2] J. J. Thomson. . Philosophical Magazine **38**, 418 (1894).

[3] G. Unlenbeck and S. Goudsmit. . Naturwissenschaften **47**, 264 (1925).

[4] P. Dirac. *The principles of quantum mechanics* (Oxford university Press, 1958).

[5] W. Thomson. . Proc. R. Soc. **8**, 546 (1857).

[6] P. Zeeman. *The effect of magnetisation on the nature of light emitted by a substance*. Nature **55**, 347 (1897).

[7] W. Gerlach and O. Stern. *Der experimentelle nachweiss der richtungsquantelung im magnetfeld*. Zeits. Phys. **9**, 349 (1922).

[8] Z. H. Xiong, D. Wu, Z. V. Vardeny, and J. Shi. *Giant magnetoresistance in organic spin-valves*. Nature **427**, 821 (2004).

[9] V. Dediu, M. Murgia, F. C. Matacotta, C. Taliani, and S. Barbanera. *Room temperature spin polarized injection in organic semiconductor*. Solid State Communications **122**, 181 (2002).

[10] D. D. Awschalom, D. Loss, and N. Samarth. *Semiconductor Spintronics and Quantum Computation* (Springer, 2002).

[11] M. Johnson and R. H. Silsbee. *Interfacial charge-spin coupling: Injection and detection of spin magnetization in metals*. Phys. Rev. Lett. **55**, 1790 (1985).

[12] F. J. Jedema. *Electrical Spin Injection in metallic Mesoscopic Spin Valves*. Ph.D. thesis, RuG (2002).

[13] Y. Ohno, D. K. Young, B. Beschoten, F. Matsukure, H. Ohno, and D. D. Awschalom. *Electrical spin injection in ferromagnetic semiconductor structure*. Nature **402**, 781 (1999).

[14] I. Malajovich, J. M. Kikkawa, D. D. Awschalom, J. J. Berry, and N. Samarth. *Coherent transfer of spin through a semiconductor heterointerface*. Phys. Rev. Lett. **84**, 1015 (2000).

[15] G. Schmidt, D. Ferrand, L. W. Molenkamp, A. T. Filip, and B. J. van Wees. *Fundamental obstacle for electrical spin injection from a ferromagnetic metal into a diffusive semiconductor*. Phys. Rev. B. **62**, R4790 (2000).

[16] R. I. Rashba. *Theory of spin injection: Tunnel contacts as a solution of the conductivity mismatch*. Phys. Rev. B. **62**, R16267 (2000).

[17] A. Fert. *Conditions for efficient spin injection from a ferromagnetic metal into a semiconductor*. Phys. Rev. B. **64**, 184420 (2001).

[18] P. M. Tedrow and R. Meservey. *Spin-dependent tunneling into ferromagnetic nickel*. Phys. Rev. Lett. **26**, 192 (1971).

[19] N. Tombros, S. J. van der Molen, and B. J. van Wees. *Separating spin and charge transport in single wall carbon nanotubes.* cond-mat **0506538**, 0 (2004).

[20] K. Hummelen. *Reader preparation of nanomaterials and devices, topmaster nanoscience, part1 Synthesis of functional molecules* (RuG, 2004).

[21] C. Mattheus. *Polymorphism and electronic properties of pentacene.* Ph.D. thesis, RUG (2002).

[22] O. D. Jurchescu, J. Baas, and T. Palstra. *Effects of impurities of single crystal pentacene.* Appl. Phys. Lett **84**, 3061 (2004).

[23] A. Schoonveld. *Transistors based on ordered organic semiconductors.* Ph.D. thesis, RUG (1999).

[24] O. D. Jurchescu, J. Baas, and T. Palstra. *Electronic transport properties of pentacene single crystals upon exposure to air.* to be published **0**, 0 (2005).

[25] J. E. Northrup and L. Chabinyc. *Gap states in organic semiconductors: Hydrogen- and oxygen-induced states in pentacene.* Phys. Rev. B. **68**, 0412021 (2003).

[26] D. Li, E. Borkent, R. Nortrup, H. Moon, H. Katz, and Z. Bao. *Humidity effect on electrical performance of organic thin-film transistors.* Appl. Phys. Lett **86**, 0421051 (2005).

[27] A. Vollmer, O. D. Jurchescu, I. Arfaoui, T. Palstra, P. Rudolf, J. Niemax, J. Pflaum, I. Salzman, J. P. Rabe, and N. Koch. *The effect of oxygen exposure on pentacene electronic structure.* to be published **0**, 0 (2005).

[28] T. Minari, T. Nemoto, and S. Isoda. *Fabrication and characterization of single-grain organic field-effect transistor.* J. Appl. Phys. **96**, 769 (2004).

[29] C. Tanase. *Unified Charge Transport in Disordered Organic Field-Effect Transistors and Light-Emitting diodes.* Ph.D. thesis, RUG (2005).

[30] P. V. Pesavento, R. J. Chesterfield, C. R. Newman, and C. D. Frisbie. *Gated four-probe measurements on pentacene thin-film transistors: Contact resistance as a function of gate voltage and temperature.* J. Appl. Phys. **96**, 7312 (2005).

[31] M. Popinciuc, H. T. Jonkman, and B. J. van Wees. *.* to be published **.**, . (2005).

[32] C. Rost, S. Karg, W. Riess, M. A. Loi, M. Murgia, and M. Muccini. *Light-emitting ambipolar organic heterostructure field-effect transistor.* Synthetic Metals **146**, 237 (2004).

[33] T. Yasuda, T. Goto, K. Fujita, and T. Tsutsui. *Ambipolar pentacene field-effect transistors with calcium source drain electrodes.* Appl. Phys. Lett **85**, 2098 (2004).

[34] N. Koch, A. Kahn, J. Ghijsen, J. Pireaux, J. Schwartz, R. L. Johnson, and A. Elschner. *Conjugated organic molecules on metal versus polymer electrodes: Demonstration of a key energy level alignment mechanism.* Appl. Phys. Lett **82**, 70 (2003).

[35] W. H. Rippard, A. C. Perrella, F. J. Albert, and R. A. Buhrman. *Ultrathin aluminum oxide tunnel barriers.* Phys. Rev. Lett. **88**, 0468051 (2002).

[36] P. R. Leclair. *Fundamental Aspects of Spin Polarized Tunneling - magnetic tunnel junctions and spin filters.* Ph.D. thesis, TUE (2002).

[37] S. Blundell. *Magnetism in condensed matter* (Oxford, 2001).

[38] F. Bakker. *Bachelor thesis: Anisotropic magnetoresistance in cobalt strips and transport phenomena in carbon nanotubes* (RUG, 2005).

[39] C. A. Ross, S. Haratani, F. J. Castan, Y. Hao, M. Hwang, M. Shima, J. Y. Cheng, B. Vogeli, M. Farhoud, M. Walsh, and H. I. Smith. *Magnetic behavior of lithographically patterned particle arrays.* J. Appl. Phys. **91**, 6848 (2002).

[40] G. V. Samsonov. *The oxide handbook* (Plenum, 1973).

[41] T. Trunk, M. Redjdal, A. Kákay, M. F. Ruane, and F. B. Humphrey. *Domain wall structure.* J. Appl. Phys. **91**, 6848 (2002).

[42] A. E. T. Kuiper, M. F. Gillies, V. Kottler, G. W. 't Hooft, J. G. M. van Berkum, C. van der Marel, Y. Tamminga, and J. H. M. Snijders. *Plasma oxidation of thin aluminum layers for magnetic spin-tunnel junctions.* J. Appl. Phys. **89**, 1965 (2001).

[43] R. Stratton. *Volt-current characteristics for tunneling through insulating films.* J. Phys. Chem. Solids **23**, 1177 (1962).

[44] A. Bezryadina, C. Dekker, and G. Schmid. *Electrostatic trapping of single conducting nanoparticles between nanoelectrodes.* Appl. Phys. Lett **71**, 1273 (1997).

[45] M. Trouwborst. *Characterization of Gold Nanocontacts Fabricated by Electromigration* (RUG, 2003).

[46] *http://mcraefamily.com/mathhelp/physicselec.htm.*

[47] H. Klauk, G. Schmid, W. Radlik, W. WEber, L. Zhou, C. D. Sheraw, J. A. Nichols, and T. N. Jackson. *Contact resistance in organic thin film transistors.* Solid State Electronics **47**, 297 (2003).

[48] C. Goldmann, S. Haas, C. Krellner, K. P. Pernstich, D. J. Grundlach, and B. Batlogg. *Hole mobility in organic single crystals measured by a flip-crystal field effect technique.* J. Appl. Phys. **96**, 2080 (2004).